A&A, 712, A222 (2026)
https://doi.org/10.1051/0004-6361/202660084

Astronomy & Astrophysics

X-Shooter survey of disc accretion in Upper Scorpius*

II. A lack of correlation between accretion rates and disc properties

A. Empey[1,**], C. F. Manara[2], R. Garcia Lopez[1], A. Natta[1,3], R. Claes[16], F. Zagaria[4,5], J. M. Alcalá[6], R. Anania[7], G. Beccari[2], J. Carpenter[8], S. Facchini[9], D. Fedele[10], G. Lodato[9], K. Mauco[2,11], A. Miotello[2], B. Nisini[12], I. Pascucci[13], L. Piscarreta[2], G. Rosotti[9], A. Scholz[14], L. Testi[15], and M. Vioque[2]

(Affiliations can be found after the references)

Received 26 March 2026 / Accepted 16 June 2026

ABSTRACT

Context. The evolution of protoplanetary discs is intertwined with the process of planet formation, growth and migration. Studies of nearby star-forming regions of different ages and properties provide the information needed to understand the processes governing their evolution.

Aims. This paper presents the results of a spectroscopic study of the stellar and accretion properties of a large sample of 127 stars with protoplanetary discs in the Upper Scorpius region, a relatively old (5–10 Myr), nearby (~145 pc) star-forming region, with disc dust masses inferred from ALMA continuum measurements.

Methods. We derived the accretion luminosity from the excess UV continuum emission with respect to the photospheric and chromospheric emission self-consistently with the stellar spectral types, extinction, and luminosity, using the FitteR for Accretion ProPErties of T Tauri stars (FRAPPE) code. We applied a new method to evaluate upper limits on the accretion luminosity. In ~50% of cases, we could only evaluate upper limits on the accretion luminosity, either because the signal-to-noise ratio of the data was insufficient or because the measured value of the accretion luminosity was below the statistical estimate of the emission due to chromospheric activity.

Results. The mass accretion rate shows a weak correlation with stellar mass, while we find no correlation with disc properties such as dust mass or gaseous disc radius. The dispersion is larger than that found in younger star-forming regions such as Lupus and Chamaeleon I, and suggests fading of the correlations with age. We find no evidence that the observed dispersion can be explained by membership in Upper Scorpius sub-groups, or by the properties of known binary systems or transition discs.

Conclusions. The lack of correlation and the large dispersion of accretion rates challenge the current expectations of evolutionary models. The observed properties point to a decoupling of the inner and outer discs by the age of Upper Scorpius and a fading of the relations observed in younger star-forming regions, which calls for further development of current theoretical frameworks to be explained.

Key words. accretion, accretion disks – protoplanetary disks – stars: pre-main sequence – stars: variables: T Tauri, Herbig Ae/Be

1. Introduction

To date, thousands of exoplanets have been discovered as a result of advances in our observational capabilities. These discoveries have significantly improved our understanding of these worlds. However, fundamental unanswered questions remain regarding how they are born and evolve. A key component in tackling these issues is to better understand how their natal environments, the protoplanetary discs, evolve (Morbidelli & Raymond 2016).

Disc properties evolve while planetary systems form and this evolution affects their final architecture and composition (Drążkowska et al. 2023). At the centre of this dramatic interplay is a young, evolving star that interacts with the disc through several accretion and ejection mechanisms critical to shaping the physical properties of the disc (Hartmann et al. 2016; Pascucci et al. 2023), until the disc itself dissipates (Alexander et al. 2014). By studying star-disc interactions, it is possible to study the mechanisms driving disc evolution.

There remains a longstanding debate about the fundamental underlying mechanisms responsible for the evolution and eventual dispersal of these discs (Manara et al. 2023). On the one hand the viscous framework attributes disc evolution to the transport of angular momentum within the disc via turbulence-induced viscosity (Lynden-Bell & Pringle 1974). On the other hand, under the prescription of the magneto-hydrodynamic (MHD) wind-driven theory, angular momentum is instead removed via magneto-thermal winds (Blandford & Payne 1982; Bai & Stone 2013; Bai 2016; Lesur 2021; Tabone et al. 2022). In addition to these basic disc-evolution processes, many additional forces contribute to disc shaping and dispersal. These include external processes such as binary encounters or flybys (Clarke & Pringle 1993; Pfalzner et al. 2005; Cuello et al. 2023), accretion of material from the environment (e.g. Gupta et al. 2023; Winter et al. 2024) and external photoevaporation (Clarke 2007; Anderson et al. 2013; Facchini et al. 2016; Winter & Haworth 2022; Maucó et al. 2023).

The key to constraining such models and developing a more complete understanding of the disc evolutionary process lies in conducting demographic studies of different star-forming regions (Lodato et al. 2017; Manara et al. 2023; Somigliana et al. 2024; Tabone et al. 2025). Given the expected ~3−10 Myr lifetime of discs (e.g. Fedele et al. 2010; Ratzenböck et al. 2023a; Delfini et al. 2025), studying regions of different characteristic ages acts as a tracer of the overarching evolutionary path.

* Based on observations collected at the European Southern Observatory under ESO programmes 097.C-0378(A), 0101.C-0866(A), 113.26NN.001, 113.26NN.003, 115.27XL.001, and 105.2082.003.

** Corresponding author: aaron.empey@gmail.com

The key properties needed to constrain disc evolution mechanisms are the stellar mass ($M_\star$) and age, the mass accretion rate ($\dot{M}_{\rm acc}$), as well as the bulk disc mass and size in gas and dust (Manara et al. 2023; Miotello et al. 2023). These bulk properties are shown to evolve with time across various star-forming regions, reflecting their age (Ansdell et al. 2017; Hendler et al. 2020). Measurements of accretion rates and dust-based disc masses show a correlation in various star-forming regions (Manara et al. 2016b; Mulders et al. 2017; Manara et al. 2020; Testi et al. 2022; Almendros-Abad et al. 2024).

The physical mechanism to explain these dependences and how they evolve with time is still debated. Population-synthesis models show that the choice of evolutionary models (viscous, wind-driven, or hybrid, that is, a mixture of the two) has an impact on the dispersion in the relations and how they change with time (Somigliana et al. 2024). Notably, the wind-driven scenario appears more favourable for explaining the scatter in the observed correlations (Somigliana et al. 2024). Recently, JWST observations of MHD winds, which allow measurements of their mass-loss rates, offer a complementary approach for testing disc evolution models (Pascucci et al. 2025). Nonetheless, more observational surveys measuring accretion and disc properties are required to constrain the underlying mechanisms behind disc evolution and dispersal in these models.

Measurements of the properties of young stars and their discs have become possible due to the advent of sensitive optical spectrographs such as X-Shooter (Vernet et al. 2011) on the European Southern Observatory's (ESO) Very Large Telescope (VLT) and millimetre interferometers – such as the Atacama Large Millimeter Array (ALMA), and the accurate distance measurements provided by the *Gaia* satellite (Gaia Collaboration 2016). The availability of these powerful instruments paved the way for large observing campaigns to probe various nearby star-forming regions including Lupus (Ansdell et al. 2016, 2018; Sanchis et al. 2020; Alcalá et al. 2014, 2017), Corona Australis (Cazzoletti et al. 2019), Taurus (Andrews et al. 2013; Akeson et al. 2019; Long et al. 2019), Chamaeleon I (Pascucci et al. 2016; Manara et al. 2016a, 2017), and ρ Ophiucus (Cox et al. 2017; Cieza et al. 2019; Testi et al. 2022). These have provided important catalogues of star and disc properties at young ages (1–3 Myr). However, these objects remain poorly characterised at older ages (>5 Myr), limiting our ability to constrain the predictions of evolutionary models (e.g., Somigliana et al. 2024; Zagaria et al. 2023).

With an estimated age range of ~5–10 Myr (Luhman 2020), Upper Scorpius (hereafter USco) is a prime candidate to fill this gap. The first ALMA surveys of the region revealed that disc dust masses were lower than in younger star-forming regions (Carpenter et al. 2014; Barenfeld et al. 2016). The spectroscopic surveys of the region available to date either lack access to the most direct tracer of accretion, UV-excess emission (e.g., Preibisch et al. 2002; Rizzuto et al. 2015; Luhman & Mamajek 2012; Fang et al. 2023; Delfini et al. 2025), or are limited to small and incomplete sample sizes (Manara et al. 2020). Nonetheless they show that the stellar, disc, accretion and wind properties have evolved by the age of USco, making larger follow-up campaigns essential.

Manara et al. (2020) – hereafter M20, based the target selection of their pilot study on the ALMA observations of Barenfeld et al. (2016), who targeted discs in the region identified from their infrared excesses. The M20 sample was highly incomplete as the objects were confined to two disc dust mass bins with the specific goal of measuring the spread of the $\dot{M}_{\rm acc}$–$M_{\rm disc}$ relation, a key tracer of disc evolution observed in younger star-forming regions (Manara et al. 2016b; Mulders et al. 2017; Lodato et al. 2017; Zallio et al. 2024). In M20, the authors derived these masses from millimetre continuum flux densities, while X-Shooter spectra allowed them to measure stellar and accretion properties. They show that the accretion and disc properties are more evolved than in younger star-forming regions (e.g. Lupus, Chamaeleon I). However, a number of objects still exhibit high accretion rates at this age. The authors also find a large spread in the values of $\dot{M}_{\rm acc}$ at a given $M_{\rm disc}$. This result is in tension with the expectations of viscous evolution theory (Lodato et al. 2017; Rosotti et al. 2017) and suggests that other factors, possibly including external photoevaporation, binarity, and dust evolution, may be relevant in USco. The follow-up studies by Sellek et al. (2020) and Zagaria et al. (2022) suggest a similar conclusion.

More recently, the ALMA Survey of Gas Evolution of Protoplanetary Disks (AGE-PRO) investigated the region (Zhang et al. 2025). Anania et al. (2025) demonstrate that the decrease in the measured gas radii of the discs in USco can be explained, in part, by the moderate level of external photoevaporation present in the region. Population synthesis models by Tabone et al. (2025) suggest that MHD wind-driven models better reproduce the disc fraction, mass, and accretion rate in USco as well as in Ophiuchus and Lupus. In contrast, Zagaria et al. (2023) and Somigliana et al. (2024) show that USco cannot be treated simply as an older counterpart to Lupus or Chamaeleon I and that any comparison must take this into account. However, in order to discriminate between the various models and address open questions about the region, observations of a large sample of discs in USco are essential. Such a sample will play an important role in addressing broader questions on the late stages of disc evolution.

Following Gaia Early Data Release 3 (EDR3) (Gaia Collaboration 2016, 2023) the population of stars in USco increased significantly (Luhman 2020). This led to ALMA observations of 284 objects showing mid-infrared (MIR) excesses (Carpenter et al. 2025), substantially increasing the disc sample. Their millimetre flux densities were used to derive disc sizes and masses for a number of these targets (Zallio et al. 2026a; Pinilla et al. 2025; Zagaria et al., in prep.). We present for the first time, X-Shooter spectra for 88 of these targets.

In this work we build upon the survey presented by M20 to obtain the stellar and accretion properties for a sample of 127 disc-bearing stars in USco. We selected objects from previous lists of USco members (Barenfeld et al. 2016; Luhman 2020; Carpenter et al. 2025). We combined X-Shooter with ALMA millimetre flux densities to derive the key stellar, accretion, and disc properties for a statistically significant sample of objects in the region. We aimed to describe the bulk properties of the USco region and investigate their relations within the context of their late evolutionary stage. With this larger sample, we provide a statistically robust description of the $\dot{M}_{\rm acc}$–$M_{\rm disc}$ relation in the region.

The paper is structured as follows. Section 2 presents the sample, the X-Shooter observations, and the data reduction. In Sect. 3 we present the analysis of the spectra and the derivation of the stellar and accretion properties. We present the results in Sect. 4. We discuss the findings and their implications in Sect. 5 before summarising and concluding in Sect. 6.

2. Sample, observations, and data reduction

2.1. Sample

In this survey we build upon the work of M20 who studied 36 target. By adding an additional 91 objects, we more than tripled the sample of disc-bearing stars in USco with measurable disc and accretion properties, to a total of 127. We included objects in a wider range of stellar and disc-mass bins, allowing for a more robust statistical analysis of the region.

We based our X-Shooter sample selection on the work of Luhman (2020), who classified stars with evidence of discs from near- and MIR excesses and identify them as likely members of USco. Their sample is included in the list of 284 objects recently observed by Carpenter et al. (2025) and, in most cases, shows detected continuum emission with ALMA Band 7 (0.8–1.1 mm). Here we present new X-Shooter observations for 91 objects from their sample that still lack broadband spectra. We include the initial 36 targets of M20 for further completeness.

The targets range in spectral type (SpT) from M6 to G9. From the full sample of 127 targets, we derived stellar and accretion parameters for 121. For the remaining six targets[1], the poor-quality X-Shooter spectra prevented us from simultaneously and accurately fitting both spectral type and accretion luminosity (see Sect. 3). We therefore exclude these targets from the analysis. From the initial M20 sample, we re-analysed the X-Shooter spectra of 35 targets for self-consistency. In one case (2MASS J16042165-2130284) we adopted the M20 parameter values, as the new version of the fitting programme (Sect. 3) also did not converge.

The study of irregular dippers in USco by Empey et al. (2025) includes seven objects also present in our sample[2]. Empey et al. (2025) show that the observed variability is a result of occultations of the stars from the disc, rather than from sudden bursts of accretion. Hence, we include them in our sample. The total sample considered in the analysis contains 121 targets.

2.2. Observations

The observations presented here were obtained with the X-Shooter spectrograph, mounted on ESO's VLT (Vernet et al. 2011). The initial 36 M20 targets were observed in service mode under Pr.Id 097.C-0378 (PI Manara) and in visitor under programme Pr.Id. 0101.C-0866 (PI Manara). The remaining 88 targets were observed in service mode programmes, Pr.Ids 105.2082.003, 111.255B.001 (PI Claes, May 2023), 113.26NN.001, 113.26NN.003 (PI Manara, May-September 2024), and P115.27XL.001 (PI Manara, May-September 2025). For all targets, spectra were obtained using both narrow and wide slit widths. The former were taken in an ABBA nodding pattern to better remove sky emission, while the latter were taken in stare mode for the most time-efficient observations. For narrow-slit observations, slit widths were set to 1.0″ or 0.5″ in the ultraviolet-blue (UVB) arm, and 0.4″ or 0.9″ for the visual (VIS) and near-infrared (NIR) arms (see Appendix Table E.1). These configurations ensured spectral resolutions of $\gtrsim$10 000 in the VIS and NIR arms ($\lambda > 500$ nm) and $\gtrsim$5500 in the UVB arm ($\lambda \sim 300-500$ nm). Wide-slit observations used a slit width of 5.0″ in all arms to ensure maximum flux gain throughout. These were used to correct the higher-resolution, narrow configuration observations for slit losses.

The observing conditions were generally good for most observing runs, with mostly clear or photospheric conditions and typical airmass-corrected seeing of ~1.0″ in the VIS. For a few cases where the conditions did not meet the requirements, we obtained repeat observations. For Pr.Id 105.2082.003, the observations of four targets were taken in thin and thick conditions with seeing ~2.0″. In visual binary systems, the slits were aligned to include both components, but in general the slits were orientated at a parallactic angle. We present the log of the observations in Appendix E.

2.3. Data reduction

We carried out standard data reduction procedures using the X-Shooter pipeline v3.6.8 (Modigliani et al. 2010) alongside the EsoReflex workflow v2.11.5 (Freudling et al. 2013). This performs the usual steps of flat, bias, and dark correction, wavelength calibration, spectral rectification, and extraction of the 1D spectra. We completed the flux calibration using a standard star observed on the same night. We performed telluric correction on all spectra using Molecfit for the VIS and NIR arms (Smette et al. 2015; Kausch et al. 2015). To correct for slit losses, we scaled the narrow-slit spectra to the wide-slit flux, as in other works (e.g. M20, Manara et al. 2021). The overall flux calibration is in good agreement with historical photometry for the majority of targets[3]. The seven targets showing significant differences exhibit evidence of ongoing variability (see Appendix B).

For several binary targets in the sample (2MASS J16064102-2455489, 2MASS J16060215-2003142, 2MASS J16054540-2023088, and 2MASS J15354856-2958551) we resolved both components. In these cases, we manually extracted the narrow- and wide-slit exposures of both components from the reduced 2D slit images using the Image Reduction and Analysis Facility (IRAF) (Tody 1986, 1993; Fitzpatrick et al. 2025). We then flux calibrated them individually. The final spectra of the fainter secondary components often have poor signal-to-noise ratios (S/N). We analysed only the spectra of the primary components, with the exception of 2MASS J15354856-2958551 (east and west) where both components show clear spectra and were identified as young stellar objects (YSOs, see M20). Additionally, due to the poor observing conditions, we were unable to resolve the two components of 2MASS J16113134-1838259 (AS 205). Hence, we excluded this target from our sample.

3. Data analysis

3.1. Derivation of stellar and accretion properties

We derived the stellar and accretion properties of the targets in the sample by analysing their spectra with the FitteR for Accretion ProPErties of T Tauri stars (FRAPPE [4]) code described by Claes et al. (2024), based on the original method of Manara et al. (2013a). The FRAPPE code uses an interpolated grid of class III

[1] The targets with no reported fits are 2MASS J16060215-2003142, 2MASS J16064102-2455489, 2MASS J16062383-1807183, 2MASS J16183317-2517504, 2MASS J16111742-1918285, and 2MASS J16083319-2015549.

[2] The dippers in our sample are 2MASS J16041893-2430392, 2MASS J16042165-2130284, 2MASS J15583692-2257153, 2MASS J16020757-2257467, 2MASS J16090075-1908526, 2MASS J16141107-2305362, and 2MASS J16154416-1921171.

[3] Due to the poor observing conditions for 4 targets in Pr.Id 105.2082.003, flux calibration was unreliable and therefore the spectra were scaled to match the historical photometry.

[4] FRAPPE GitHub: https://github.com/RikClaes/FRAPPE.git

templates to derive spectral properties with an improved fitting method.

The code reproduces an input spectrum by using three main components: (a) continuum slab models to describe the excess continuum emission from the accretion shock, (b) a reddening law to account for extinction, and (c) a grid of interpolated class III templates to reproduce the stellar photospheric and chromospheric emission.

The isothermal hydrogen slab models developed in Rigliaco et al. (2012), Manara et al. (2013b), and described in Manara (2014), are used to reproduce the excess UV emission in spectra due to accretion. The models are matched to the de-reddened observed spectra through a scaling factor that is used in the calculation of the total accretion flux. The extinction is determined by incorporating the Cardelli reddening law (Cardelli et al. 1989). The total-to-selective extinction ratio is fixed to the commonly accepted interstellar value of $R_V = 3.1$, while exploring a range of input extinction magnitudes (A_V) to determine the best fit. The stellar contribution is found by comparing the de-reddened observed spectrum with a grid of interpolated class III templates (see Claes et al. 2024 for details) ranging from SpT G8 to M9.5. The code applies a scaling factor to the template to correct for distance and stellar luminosity, and aims to reproduce the observed flux at key regions of the spectra. Under this approach, the spectral type determination is typically accurate to within half of a subclass; however, the uncertainties can be larger at the edge of the grid (i.e. for earlier SpTs).

The fitter is ran with a set of input spectral types, range of extinction magnitudes (A_V) and on the whole grid of slab models, and determines the best fit by minimizing a $\chi^2_{\rm like}$ likelihood function. The SpT is used to obtain the effective temperature ($T_{\rm eff}$) via the relations of Herczeg & Hillenbrand (2014). The stellar luminosity ($L_\star$) is then computed from $L_\star = 4\pi d^2 F_{\rm bol}$, where d is the distance to the target and $F_{\rm bol}$ is the stellar flux at 751 nm with the bolometric correction of Herczeg & Hillenbrand (2014), Claes et al. (2024). By placing these measurements on the HR diagram the stellar age and mass are derived by interpolating between evolutionary tracks. We report the values derived from the tracks of Baraffe et al. (2015), with the exception of one target (2MASS J15583692-2257153, highest $T_{\rm eff}$ in Fig. 1) for which we use those of Siess et al. (2000) as it lies outside the parameter range of the Baraffe tracks.

The accretion luminosity is computed from the slab model flux ($F_{\rm acc}$) integrated over frequency ($L_{\rm acc} = 4\pi d^2 F_{\rm acc}$). The corresponding mass accretion rate is then given by $\dot{M}_{\rm acc} = 1.25 L_{\rm acc} R_\star/(GM_\star)$ (Gullbring et al. 1998). We report the derived properties from FRAPPE for all objects in the sample in Appendix Table D.1 (see Claes et al. 2024 for more details). As the fitter does not report individual uncertainties on the measured values, we include typical uncertainties on the key properties[5]. We took parallactic distances (d) for each target from the Gaia EDR3 catalogue of Bailer-Jones et al. (2021).

Figure 1 shows the HR diagram of this sample, with one object exhibiting a very low $L_\star$ for its associated $T_{\rm eff}$: 2MASS J16020429-2231468. It is likely that this object was observed in a period of variability (see Appendix B) and so we excluded it from further analysis. The figure also shows that the majority of our targets fall between the 3–10 Myr isochrones of the evolutionary models of Baraffe et al. (2015). This is generally in line with the expected typical age of the USco region (~5–10 Myr). Seven objects fall below the 10 Myr line, with multiple showing

[5] Typical uncertainties are as follows: $\sigma L_\star = 0.2$ dex, $\sigma M_\star = 0.1$ dex, $\sigma L_{\rm acc} = 0.2$ dex, $\sigma \dot{M}_{\rm acc} = 0.35$ dex.

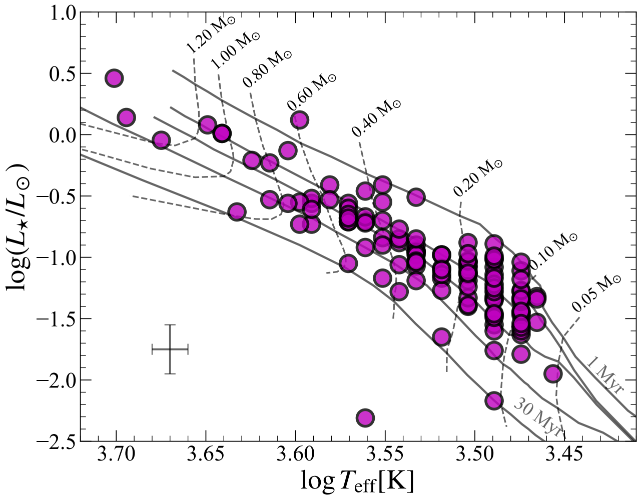

Fig. 1. Hertzsprung-Russel (HR) diagram for the sample of disc-bearing stars in USco. The black lines show the Baraffe et al. (2015) evolutionary tracks (dashed) with isochrones (solid), corresponding to ages of 1, 3, 5, 10, and 30 Myr. The grey cross in the lower-left corner represents the typical uncertainties of $L_\star$ (0.2 dex) and of $T_{\rm eff}$ (0.01 dex).

isochronal ages up to 31 Myr. The median isochronal age of the sample is 3.74 Myr; however, this value depends on the choice of evolutionary model (Fang & Herczeg 2025; Zallio et al. 2026b). Dynamical mass measurements can also be used to help constrain disc ages (Towner et al. 2026; Zallio et al. 2026b). However, we did not use individual target ages in this analysis.

3.2. Upper limits and chromospheric emission

Across the sample we find a significant fraction of objects with notably low accretion luminosities (i.e. $L_{\rm acc} \lesssim 10^{-4} L_\odot$). At this level, measuring a true accretion luminosity (due to a continuum excess) may be complicated by emission from the stellar chromosphere or by low S/N in the spectra at $\lambda < 360$ nm. Although FRAPPE can fit these targets, the current version does not estimate individual uncertainties on its $L_{\rm acc}$ measurement (Claes et al. 2024). Therefore, we introduced a criterion to separate definite accretors from targets for which the excess is uncertain, and for the latter we estimated 1σ upper limits of the accretion measurements. In brief, the method distinguishes objects based on the S/N of the observed spectra in the four bins of the Balmer continuum used by FRAPPE to determine the excess emission due to accretion. We provide more details of this method in Appendix A. Using this approach, we classify a total of 49/121 (40%) objects as upper-limit measurements.

T Tauri stars are known to have active chromospheres (Houdebine et al. 1996; Franchini et al. 1998; Stelzer et al. 2013), whose emission can contaminate measurements of accretion luminosity (Ingleby et al. 2011; Rigliaco et al. 2012). To investigate this effect, we compared the $L_{\rm acc}/L_\star$ ratio of our objects to typical chromospheric emission levels of class III stars of the same spectral type (Manara et al. 2013b, 2017, see Fig. 2). This comparison provides a simple check to flag objects whose $L_{\rm acc}$ measurements may be affected by chromospheric emission. We find that 29 targets in the sample lie on or below this threshold. These targets predominately populate the lowest measured accretion luminosity range ($L_{\rm acc} \lesssim 10^{-4} L_\odot$). Therefore, any measured continuum excess may not be due solely to ongoing accretion, but may be contaminated by chromospheric

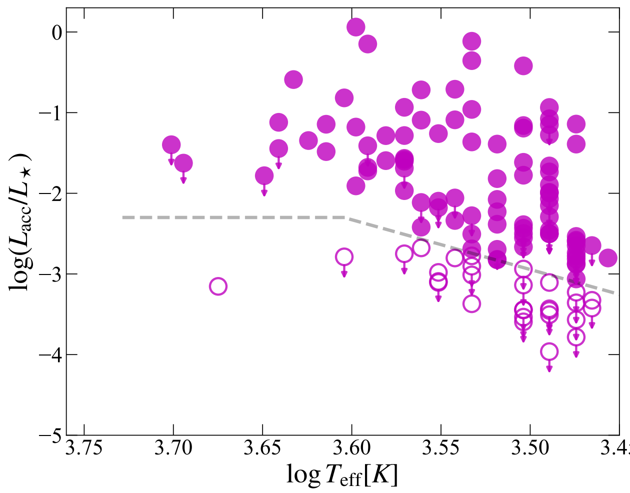

Fig. 2. Accretion-to-stellar luminosity ($L_{\rm acc}/L_\star$), as a function of effective temperature ($T_{\rm eff}$). The dashed grey line shows the chromospheric emission limit derived by Manara et al. (2013b). Objects having a ratio equal to or below this line may be contaminated by chromospheric emission and are shown with hollow markers. Upper limits (Sect. 3.2) are indicated with downward-facing arrows.

emission (Manara et al. 2017). Previous works have considered such targets to be possible non-accretors (Alcalá et al. 2014, 2017; Manara et al. 2016b, 2017, 2020; Almendros-Abad et al. 2024).

Of the 29 objects whose ratios fall below the chromospheric emission limit, 19 also have upper limit accretion measurements from their low Balmer continuum excess (S/N). The remaining ten form an interesting sub-sample with well-measured continuum excesses that are, however, below the chromospheric limit for their spectral type. This is possible if the photospheric template used in the analysis has lower chromospheric noise than typical YSOs or the target star has an anomalously high level of chromospheric activity.

For simplicity we henceforth categorise the objects in our sample into two groups: definite accretors and upper-limit accretors. There is an approximately even split between these two categories, with 62 and 59 targets, respectively. The former are characterised by a clear UV continuum excess and have accretion luminosities above the chromospheric activity limit for their SpT (filled markers and no arrows in Fig. 2). We classify the remaining objects upper-limit accretors; this can occur because their spectra show no excess with respect to the interpolated Class III template, poor S/N in the UV, or because the measured accretion luminosity falls below the chromospheric activity threshold. In the following sections they are treated as censored data in all statistical analysis.

3.3. Complementary ALMA data

We computed the disc dust masses of the entire sample from the ALMA Band 7 continuum flux densities reported by Carpenter et al. (2025). The resulting values are reported in Table D.1. As in previous studies, and mindful of the many caveats (e.g. Miotello et al. 2023), we used this information as a tracer of disc dust mass. To convert the flux densities to dust masses, we assumed isothermal, optically thin dust emission from the disc following the approach of Barenfeld et al. (2016). Using distances from Gaia EDR3 (as mentioned in Sect. 3) we estimated the dust temperature profile with a Planck function with characteristic temperature, T_d. In this study we adopted the stellar luminosity scaling relation $T_d = 25K \times (L_\star/L_\odot)^{0.25}$. We used the $L_\star$ values derived in this work. We note that our results do not change if we assume a fixed temperature of $T_d = 20$ K, as is done in other studies. We computed total disc masses, hereafter referred to as $M_{\rm disc}$ for simplicity, assuming the standard 1:100 dust-to-gas ratio (i.e. $M_{\rm disc} = 100 \cdot M_{\rm dust}$). This ratio is commonly assumed in the literature, but assumes little evolution with time in discs. We discuss this aspect in Sect. 5. Four targets[6] were flagged as having unreliable millimetre flux densities from ALMA; as a result we did not include them in the analysis of disc masses.

In addition, Zagaria et al. (in prep.) derive CO disc radii for a total of 90 discs from the ALMA data of Carpenter et al. (2025). We include the median, 16th percentile and 84th percentile values of the 90% CO flux radii for 73 targets in our sample (see Sect. 4). We also include the disc structure classifications derived from the ALMA observations of Carpenter et al. (2025), Pinilla et al. (2025), Vioque et al. (2025) for the corresponding targets in our sample.

Table 1. Results of the power-law fits to relations between stellar, disc and accretion properties.

Relation	Upper Scorpius best fit parameters			
y–x	α	β	σ	ρ
$L_{\rm acc}$–$L_\star$	−1.6 ± 0.4	2.1 ± 0.4	1.4 ± 0.7	0.5 ± 0.1
$\dot{M}_{\rm acc}$–$M_\star$	−9.1 ± 0.3	2.4 ± 0.5	1.3 ± 0.6	0.5 ± 0.1
$\dot{M}_{\rm acc}$–$M_{\rm disc}$	−6.9 ± 0.9	1.1 ± 0.3	1.5 ± 0.7	0.4 ± 0.1
$\dot{M}_{\rm acc}$–$R_{\rm CO}$	−10.4 ± 1.4	0.0 ± 0.8	1.5 ± 0.8	0.0 ± 0.1
$M_{\rm dust}$–$M_\star$	0.7 ± 0.1	0.8 ± 0.1	0.5 ± 0.2	0.4 ± 0.1

Notes. The relations are always in the form $\log_{10} y = \alpha + \beta \log_{10} x$. σ measures the dispersion from the fit, ρ is the correlation coefficient where a value of 1 represents a perfect correlation and 0 signifies no correlation (see *linmix* docs). The fit of each relation is shown in Figures 3, 4, 5, 6 and Appendix Fig. C.2. The fits are based on the values reported in Table D.1, for which stellar properties were derived using the evolutionary tracks of Siess et al. (2000), Baraffe et al. (2015).

4. Results

This section summarises the derived stellar, disc, and accretion properties of the sample before exploring several key relations ($L_{\rm acc}$–$L_\star$, $\dot{M}_{\rm acc}$–$M_\star$, $\dot{M}_{\rm acc}$–$M_{\rm disc}$, and $\dot{M}_{\rm acc}$–$R_{\rm CO}$) for the disc-bearing objects in USco. We report the measurements of the stellar, accretion and disc properties for the sample in Appendix Table D.1. The large number of upper-limit measurements makes it difficult to accurately determine statistically meaningful medians and quantiles for the measured properties (see Appendix C). We therefore focused our analysis primarily on the observed scatter and on fitting the relations with a power law, as was done in similar studies of other star-forming regions. We determined the best-fit power law using the *linmix* Python package, which implements the hierarchal Bayesian linear regression method described by Kelly (2007). This approach allowed us to include upper limits in the fitting procedure. Table 1 displays the best fit parameters.

[6] The targets with unreliable millimetre flux density measurements are: 2MASS J16185382-2053182, 2MASS J16120505-2043404, 2MASS J16064385-1908056, and 2MASS J15442550-2126408.

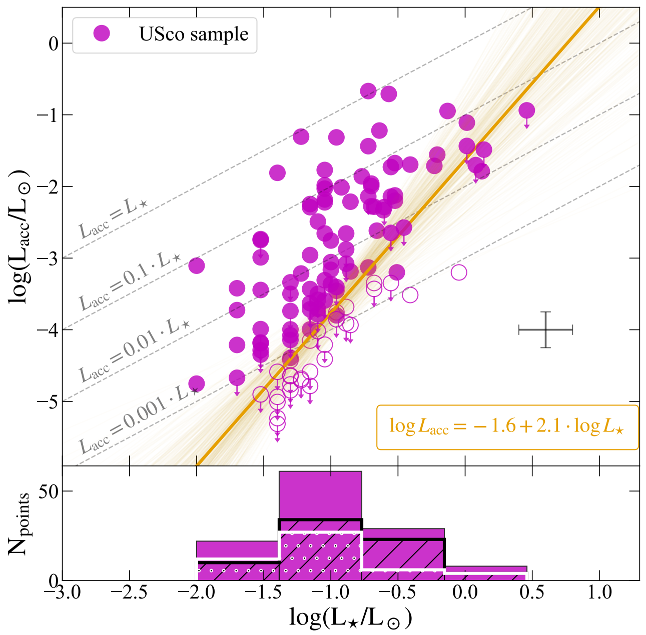

Fig. 3. Top panel: Accretion luminosity (L_{acc}) as a function of stellar luminosity ($L_\star$). Solid magenta points are definite accretors, and those with downward-pointing arrows indicate upper limit measurements based on their continuum excess. Hollow magenta points indicate targets with $L_{acc}/L_\star$ ratios below the chromospheric limit (see Fig. 2). Overplotted in orange is the best fitting power law shown in the textbox (determined by *linmix*, see Table 1 for full fit parameters and uncertainties). Faded coloured lines show sample fits taken from the Bayesian posterior (Kelly 2007). Dashed grey lines show different fixed dependencies of L_{acc} on $L_\star$ to guide the eye. The grey cross represents typical uncertainties in L_{acc}, and $L_\star$. Bottom panel: Histograms of the full sample (magenta), upper-limit accretors (white dotted), and definite accretors (black striped) in each $L_\star$ bin.

4.1. Accretion-stellar luminosity relation

Figure 3 shows the distribution of accretion luminosity as a function of stellar luminosity. The plot shows measurements of definite accretors as solid magenta points, and those of upper limit accretors with arrows and/or hollow points. Hollow points represent objects whose $L_{acc}/L_\star$ ratio falls below the expected chromospheric activity limit. The histogram shows that the proportion of upper limits to definite detections is approximately 50:50 in all bins. The upper-limit accretors are distributed across the full $L_\star$ range. As expected, the majority are among the lowest values of accretion luminosity in the sample. In contrast, several objects show very high accretion luminosities ($L_{acc} \sim L_\odot$). This demonstrates the wide range of accretion levels among the targets in the sample. In the central $L_\star$ bin ($-1.3 \leq \log(L_\star/L_\odot) \leq -0.7$), we observe a large vertical spread in L_{acc}, that spans approximately four orders of magnitude. In general, with the exception of the highest $L_\star$ values, L_{acc} shows a significant spread across all bins. In Fig. 3, we also observe a cut-off at around $\log(L_\star/L_\odot) \approx 0$, indicating a lack of objects with solar luminosity or higher.

To further evaluate this relation we fitted the scatter with a power-law relation (solid orange line in Fig. 3). The effect of the upper-limit values on the fit is evident from the best-fit curve passing through the lower envelope of the scatter. We measure a slope (β) of 2.1 ± 0.4, indicating a relatively strong dependence of the accretion luminosity on the stellar luminosity. However, the fitting procedure returns a correlation coefficient (ρ) of 0.5 ± 0.1, suggesting a moderate positive relation. The large dispersion (σ) of 1.4 ± 0.7 is also consistent with this interpretation. Given the large spread in L_{acc}, this is unsurprising. Overall, although there appears to be a relatively strong dependence of the accretion luminosity on stellar luminosity, the combination of a large spread and low correlation coefficient makes this result uncertain.

4.2. Mass accretion rate-stellar mass relation

Figure 4 shows the mass accretion rate as a function the stellar mass.[7] As highlighted by the histogram at the bottom of the plot, upper limits on $\dot{M}_{acc}$ are present across all $M_\star$ bins, but their fraction relative to definite detections is higher in the lower $M_\star$ bins. We observe a very large spread in $\dot{M}_{acc}$ at all values of $M_\star$. This spread reaches just over three orders of magnitude in the two central $M_\star$ bins. Despite this, the sample shows evidence of an increasing trend in $\dot{M}_{acc}$ with increasing $M_\star$.

To quantify this trend and facilitate comparison with results obtained in other star-forming regions, we fitted the data with a power law, using the same approach as for L_{acc}–$L_\star$. As expected, the fit is significantly influenced by the large number of upper limits throughout the sample. The fitting procedure returns a best-fit value of $\beta = 2.4 \pm 0.5$, indicating a strong dependence and therefore relation between the two properties. Figure 4 also includes a $\dot{M}_{acc} \propto M_\star^2$ relation for context, as this has been observed in other star-forming regions (e.g. Hartmann et al. 2016). Comparison with our best-fit power law shows little difference. The dispersion of the points around the fit (σ) is also significant (see Table 1), with a value of 1.3 ± 0.6. Together with a moderate correlation coefficient ($\rho = 0.5 \pm 0.1$), this again indicates an uncertain dependence driven by the large spread in $\dot{M}_{acc}$. The fit also returns $\alpha = -9.1 \pm 0.3$.

The measured slopes are consistent with previous values (e.g. Hartmann et al. 2016; Manara et al. 2023, and references therein), but the correlation is weaker than previously found. Furthermore, the targets in the upper envelope of Fig. 4 may also be consistent with a double power law fit, in which $\dot{M}_{acc}$ depends more strongly on lower $M_\star$ objects than those with $M_\star \geq 0.2\,M_\odot$($\log M_\star \approx -0.7$). This behaviour was predicted by Vorobyov & Basu (2009), and is observed in other star-forming regions (e.g., Alcalá et al. 2017; Manara et al. 2017). However, given the significant spread in the sample, we did not attempt to fit this here. We further discuss the $\dot{M}_{acc}$–$M_\star$ relation in comparison with other regions in Section 5.

4.3. Mass accretion rate-disc mass relation

Figure 5 shows the relation between the mass accretion rate and the disc dust mass. As previously mentioned, we excluded four targets flagged by Carpenter et al. (2025) as having unreliable ALMA millimetre fluxes. We also excluded one object, 2MASS J16160448-2932400, which has only an upper-limit disc dust measurement that is the lowest in the sample ($\log(M_{disc}/M_\odot) < -5.0$).

The histogram shows that upper-limit accretors are distributed across the full range of M_{disc}, with a higher fraction at the lowest disc masses. As in the previous cases, we also

[7] We note that the results for this relation can depend on the adopted evolutionary tracks used to derive the stellar mass (e.g. Betti et al. 2023; Almendros-Abad et al. 2024). As previously mentioned, we used the values reported in Appendix Table D.1, which are based on the tracks of Siess et al. (2000), Baraffe et al. (2015).

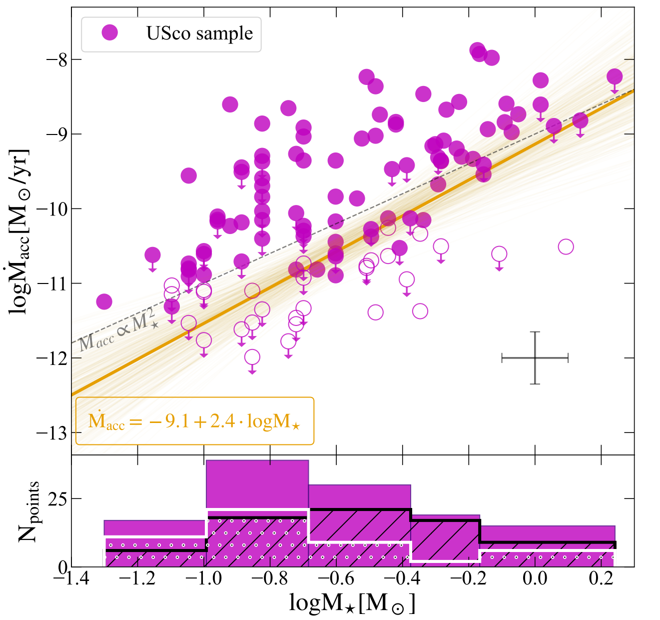

Fig. 4. Top panel: Mass accretion rate ($\dot{M}_{acc}$) plotted as a function of stellar mass ($M_\star$). Symbols and power-law fit are as in Fig. 3. The dashed grey line shows the $\dot{M}_{acc} \propto M_\star^2$ relation to guide the eye. The grey cross represents typical uncertainties in $\dot{M}_{acc}$ and $M_\star$. Bottom panel: Histograms of the full sample (magenta), upper-limit accretors (white dotted), and definite accretors (black striped) in each $M_\star$ bin.

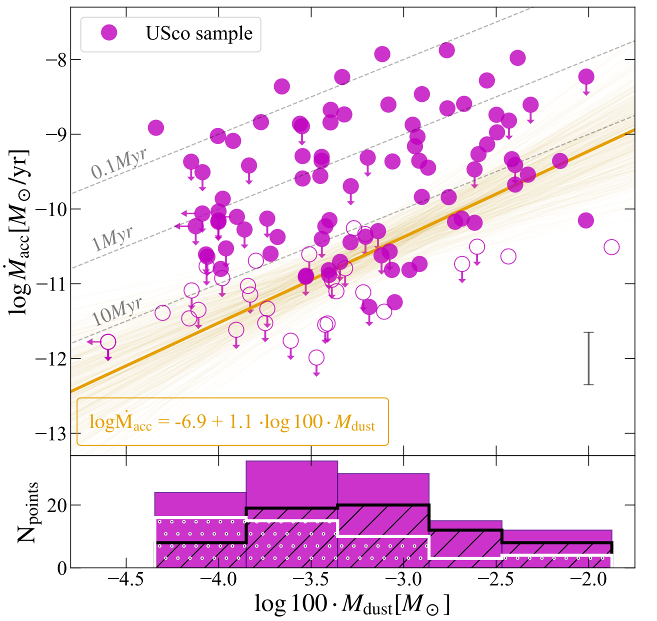

Fig. 5. Top panel: Mass accretion rate ($\dot{M}_{acc}$) as a function of disc mass (M_{disc}). Symbols and power-law fit are as in Fig. 3. The dashed grey lines indicate $M_{disc}/\dot{M}_{acc}$ ratios of 0.1, 1, and 10 Myr. The grey error bar indicates the typical uncertainty in $\dot{M}_{acc}$. Bottom panel: Histograms of the full sample (magenta), upper limit accretors (white dotted), and definite accretors (black striped) in each M_{disc} bin.

observe a large spread in $\dot{M}_{acc}$ at all values of M_{disc}. The spread is roughly consistent across all M_{disc} bins (approximately 3 dex). Given this spread, there appears to be no relation between the disc dust mass and the accretion rate. The points also do not follow any of the three dashed grey lines representing disc lifetimes ($\tau_{disc} = M_{disc}/\dot{M}_{acc}$) 0.1, 1, or 10 Myr. The large spread of the data around these lines at the age of USco is in contrast with the expectations of viscous evolution. We discuss this further in Section 5.

Due to the consistently large scatter across all M_{disc} values, the best-fit power law shown in Fig. 5 is unconvincing. The line passes through the points just below, and almost parallel to, the 10 Myr τ_{disc} line, and is once again heavily influenced by the number of upper limit accretors. It yields a best fit slope of β = 1.1 ± 0.3, consistent with previous findings (e.g. Manara et al. 2016b; Mulders et al. 2017). However, given the large dispersion (σ = 1.5 ± 0.7) and low correlation coefficient (ρ = 0.4 ± 0.1), this indicates a very weak $\dot{M}_{acc}$–M_{disc} dependence.

4.4. Mass accretion rate-radius relation

Zagaria et al. (in prep.) measured gas disc sizes for 73 targets in our sample from the integrated intensity maps of CO (J = 3–2) emission. Figure 6 shows the relation between the mass accretion rate and the CO disc radius. As in the previous relations, we observe a significant spread in $\dot{M}_{acc}$ at all disc sizes. This suggests that there is no trend between $\dot{M}_{acc}$ and R_{CO}. However, the sample contains a few objects with only an upper limit on their CO radii, as well as some with significant error bars. Therefore, it is possible that these errors could mask a correlation between the two properties. Even if this were the case, a large spread in $\dot{M}_{acc}$ values would remain.

The parameters of the best-fit power law are consistent with this interpretation, given the large dispersion and uncertainties. The slope has a value of β = 0.0 ± 0.8, indicating that a weak correlation could be present, although it is more likely that there is none. The correlation coefficient is the lowest in the sample, with a value of ρ = 0.0 ± 0.1, indicating no evidence of correlation even when the uncertainties are taken into account. The absence of a clear relation, together with the spread in $\dot{M}_{acc}$ (around four orders of magnitude), suggests that the amount of material accreted onto a star is not related to the size of the disc.

5. Discussion

5.1. Upper Scorpius membership and subgroups

Since we selected the X-Shooter sample for this work, the catalogue of disc-bearing stars believed to be members of USco has been updated. Recent studies have relied on further analysis of Gaia data (Gaia Collaboration 2023) to better constrain the membership of objects to different star-forming regions and even in their subgroups. In particular, Ratzenböck et al. (2023b) suggest that 13 objects in our sample are members of ρ Ophiucus (L1688). A further 11 objects were not included in their analysis, and therefore were not linked to any of the USco subgroups. We tested whether their inclusion in our analysis affected our results and find that it did not. First, the 24 potential non-members are distributed similarly to the other objects on the HR diagram. Moreover, we recomputed the power law fits for the $\dot{M}_{acc}$ versus $M_\star$ and $\dot{M}_{acc}$ versus M_{disc} relations presented in Sect. 4 using the reduced sample of 97 bona fide members. The resulting fit parameters are very similar to those listed in Table 1, with all differences well within the uncertainties. In particular, the correlation coefficient ρ, remains essentially unchanged.

Ratzenböck et al. (2023b) applied their `SigMA` clustering algorithm to the entire Scorpius-Centaurus OB association, and found that USco can be divided in to 9 distinct subgroups. Using Gaia DR3 data for stars in this region, they identified

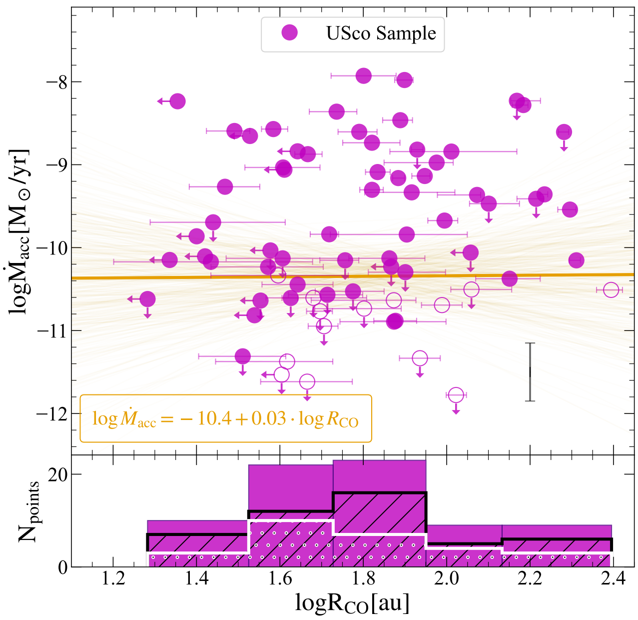

Fig. 6. Top panel: Mass accretion rate ($\dot{M}_{\rm acc}$) as a function of gas CO disc radius ($R_{\rm CO}$). Values of $R_{\rm CO}$ are taken as the median 90% CO flux radii from Zagaria et al. (in prep.), with uncertainties given by the 16th and 84th percentiles of the size distributions. In some cases these are smaller than the size of the points. Symbols and power law fit are as in Fig. 3. Horizontal and vertical arrows indicate targets for which the reported $R_{\rm CO}$ or $\dot{M}_{\rm acc}$ value is an upper limit. The grey error bar represents the typical uncertainty in $\dot{M}_{\rm acc}$. Bottom panel: Histograms of the full sample (magenta), upper limit accretors only (white dotted), and definite accretors only (black striped) in each $R_{\rm CO}$ bin.

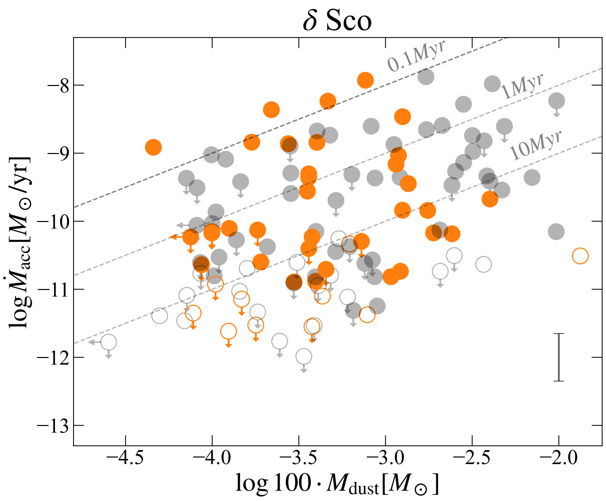

Fig. 7. $\dot{M}_{\rm acc}$ as a function of $M_{\rm disc}$ for the most abundant USco subgroups in our sample detected with Gaia (Ratzenböck et al. 2023b). A total of 112 objects in our sample were are associated with eight subgroups in the region. The sample sizes in each range between 1–45 objects; here we highlight the objects associated with the δ Sco group (orange points, 45 objects). The remaining objects in our sample are shown in grey. The grey error bar represents the typical uncertainty in $\dot{M}_{\rm acc}$.

groups based on their positions and radial velocities. We find that objects in our sample belong to eight of these groups, while the remaining 11 were not included in their study. As discussed above, one of these is ρ Ophiuchus (L1688). The most populous subgroup in USco, δ Sco, is also the most abundant subgroup in our sample containing a total of 46 objects. The next three most populous subgroups in our sample are ν Sco, ρ Ophiuchus (L1688), and β Sco containing 18, 13, and 12 objects respectively.

To investigate the effects of subgroup membership on our results we first examined whether the subgroups have different characteristic ages. We calculate the mean isochronal age for each subgroup and find that δ Sco is the oldest (5.68 Myr), followed by ν Sco (5.18 Myr), β Sco (5.10 Myr), and finally ρ Oph (4.7 Myr). This sequence of ages is broadly consistent with that reported by Ratzenböck et al. (2023a); the only difference is that they identify β Sco as having the second oldest age. However, our measured ages, derived using the Baraffe et al. (2015) evolutionary tracks, are ~2.5 Myr younger for two of the three 'Sco' subgroups discussed. We also observe a large spread in ages within each subgroup in our sample, making any measurement of a characteristic age uncertain.

We also investigated the location of objects from each subgroup in the $\dot{M}_{\rm acc}$–$M_{\rm disc}$ plot. For each subgroup, the objects approximately span the full $M_{\rm disc}$ range. Figure 7 highlights δ Sco objects in the $\dot{M}_{\rm acc}$–$M_{\rm disc}$ distribution of our full sample. Although several of the high accretors belong to this group, we find no evidence that subgroup membership explains the large spread observed in our sample. We do observe minor differences in mass accretion rates among the other three example subgroups. The spread in $\dot{M}_{\rm acc}$ may be larger for δ Sco than for ν Sco, but the small sample size of the latter makes it is difficult to confirm. If true, this could imply a correlation between the subgroup age and the spread in $\dot{M}_{\rm acc}$ values, potentially mirroring that seen between different star-forming regions. However, drawing any conclusions on the effect of subgroup membership is again limited by the small sample sizes for most subgroups.

5.2. *The accretion properties of young stars in Upper Scorpius*

In Sect. 3.2 we assigned upper limits to the accretion measurements for almost half of our sample. This allowed us to classify the sample two groups: definite accretors and upper-limit accretors. Definite accretors show clear evidence of a UV continuum excess due to accretion. Upper-limit accretors, however, show no evidence of a UV continuum excess (within the S/N of their spectra) or have measured values below the statistical estimate of the chromospheric activity of the star. For these objects accretion may still occur below what we can measure, but their discs may also have ceased accretion. As in M20, were therefore discuss these objects as potential non-accretors, while acknowledging that may still undergo low levels of accretion.

The separation between definite accretors and potential non-accretors clearly highlights the large dispersion in $L_{\rm acc}$ and, consequently, $\dot{M}_{\rm acc}$ at all stellar masses and disc dust masses. The spread is also not confined to a particular range of stellar or disc properties. The fraction of potential non-accreting targets in this work (approximately half of the sample) is significantly higher than that reported in M20 and previous studies of star-forming regions. This implies that the fraction of accreting stars (51%) is significantly lower than the fraction of stars showing near-to-mid infrared excess (100%, as per our selection criteria). This large fraction may be a signature of the late stages of disc evolution. Fedele et al. (2010) found that the fraction of accreting discs decreases with age and is smaller than the fraction of discs that show an infrared excess. They attributed this behaviour to the faster clearing of the inner gaseous disc, traced by accretion, relative to the rest of the dusty disc traced by IR-excess.

Furthermore, they estimated an accretion timescale of approximately 2.3 Myr, and found no evidence of ongoing accretion beyond 5 Myr. We derive a longer average accretion time scale ($\tau_{acc} = M_{disc}/\dot{M}_{acc}$) of 5.3 Myr. Given the older age of USco and the number of potential non-accretors in our sample, many of these discs may have ceased accreting, which is what we are seeing.

Although the sample shows clear signs of ageing, with 49% of objects having low accretion luminosities a number of objects remain at the opposite end of the scale. Fig. 3 shows that the accretion luminosities span almost five orders of magnitude within a given stellar-mass bin, with the strongest accretors having $L_{acc} \approx L_{\star}$. Such high luminosities are comparable to those observed in younger star-forming regions, and show that the picture in USco is not so clear.

In Sect. 5.4, we show that the highest mass accretion rates in USco are comparable to those of stars with the same stellar or disc mass as those in the younger Chamaeleon I (2.8 Myr) and ρ Ophiuchus (1 Myr) star-forming regions. However, the upper envelope of $\dot{M}_{acc}$ values in our sample, is generally lower than the highest from the other regions. Nonetheless, these high values suggest that there is a real dispersion in the activity of discs in USco. Strong accretors at old ages have also been observed in other regions (e.g. Ingleby et al. 2014; Rogers et al. 2025) and their existence remains an open question for current theoretical frameworks. We discuss one possible explanation in the next section.

5.3. Effect of binarity and disc structures

Previous studies have shown that different types of objects occupy different regions of the $\dot{M}_{acc}$–M_{disc} plot and may partly explain the observed spread. For example, Zagaria et al. (2022) show that, using measured accretion rates from Lupus, Chameleon I and USco, discs in binary systems tend to have higher mass accretion rates, leading to observationally estimated $\tau_{acc} \approx 0.1$ Myr. In Figure 8, we highlight objects in our sample that are either confirmed binaries (including those in Zagaria et al. 2022, mainly from Barenfeld et al. 2019) or suspected of having a close companion (Barenfeld et al. 2019; Xie et al. 2026). Although two points lie close to the 0.1 Myr accretion-timescale line, the sample here spans accretion rates spanning from $\sim 10^{-11}$–10^{-9} $M_{\odot}$/yr and accretion timescales of $\tau_{acc} \approx 0.1$–10 Myr. The low sample size (11 objects) makes it difficult to draw firm conclusions, but the spread of these points suggests that the higher $\dot{M}_{acc}$ values in the sample cannot be explained by available information on binarity. As the sample of binaries is certainly incomplete, future efforts to determine the binarity of the targets could better test this hypothesis.

Transition disc objects are characterised by an optically thin inner disc (an inner hole or cavity, seen as a dip in the MIR of their spectral energy distribution) while maintaining excess emission at longer infrared wavelengths (>10 µm) from the outer disc (e.g. Espaillat et al. 2014; van der Marel 2023). Najita et al. (2007, 2015) demonstrated that transition discs occupy the higher M_{disc} but lower $\dot{M}_{acc}$ regions of such diagrams, as also observed in other studies (e.g. Manara et al. 2016b; Mulders et al. 2017). On the other hand, the difference is smaller when considering the dependence of accretion on stellar mass (Manara et al. 2014). Follow-up studies comparing observations with planetary synthesis models show that the lower $\dot{M}_{acc}$ at a given M_{disc} could be attributed to the formation of giant planet(s) within the cavities of such discs (Manara et al. 2019). The identified transitional and structured discs in the sample

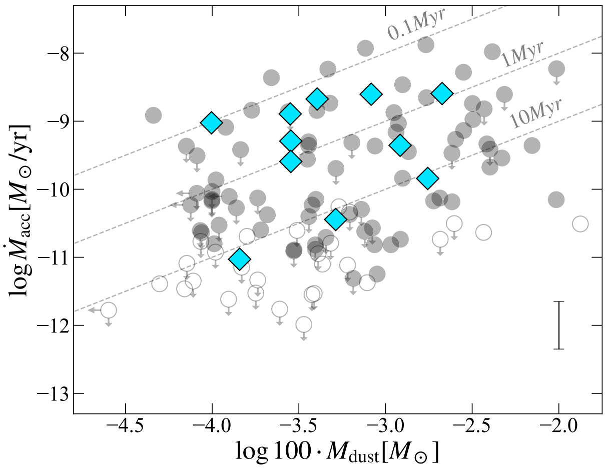

Fig. 8. $\dot{M}_{acc}$ as a function of M_{disc}, with binary targets highlighted. Cyan diamonds represent known binaries present in the sample. We also indicate potential binary systems in the sample identified by Barenfeld et al. (2019) and Xie et al. (2026). The grey error bar represents the typical uncertainty in $\dot{M}_{acc}$.

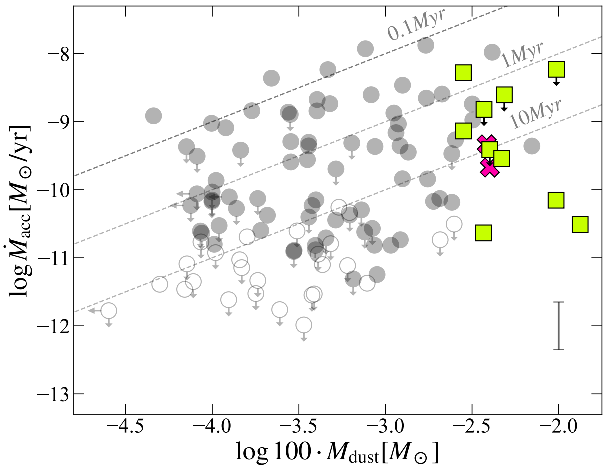

Fig. 9. $\dot{M}_{acc}$ as a function of M_{disc}, with transition and structured discs. Transition discs are shown as lime squares and structured discs (evidence of disc substructures) as pink crosses (see Carpenter et al. 2025; Pinilla et al. 2025). The grey error bar represents the typical uncertainty in $\dot{M}_{acc}$.

(Carpenter et al. 2025; Pinilla et al. 2025) have the highest disc masses (Fig. 9). This is expected because of a selection bias, as we cannot yet resolve the inner cavities of less massive discs. The $\dot{M}_{acc}$ values are again widely distributed within this sample. Interestingly, four of these objects have upper-limit measurements, suggesting that the true average $\dot{M}_{acc}$ may be lower, although it would still not reach $\tau_{acc} \sim 0.1$ Myr. This suggests that the accretion properties of the transition discs do not differ from those of the other objects in the sample. Comparison with other star-forming regions (Figures 10, 11) places these transition discs at intermediate M_{disc} and $\dot{M}_{acc}$.

These results tentatively suggest that the extremes of the $\dot{M}_{acc}$ distribution in USco cannot be explained by the general properties of binary and transitional-disc objects. However, both cases have small sample sizes, making it difficult to draw firm

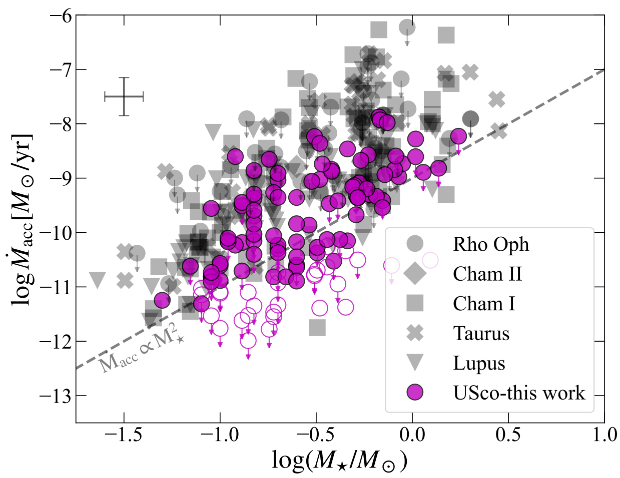

Fig. 10. $\dot{M}_{\rm acc}$ as a function of $M_\star$ for this sample, alongside values for the younger star-forming regions: ρ Ophiuchus (L1688), Chamaeleon (Cham) I and II, Lupus, and Taurus. Data are from Manara et al. (2023). The dashed grey line shows the relation $\dot{M}_{\rm acc} \propto M_\star^2$ to guide the eye. The grey cross represents typical uncertainties in $\dot{M}_{\rm acc}$, $M_\star$.

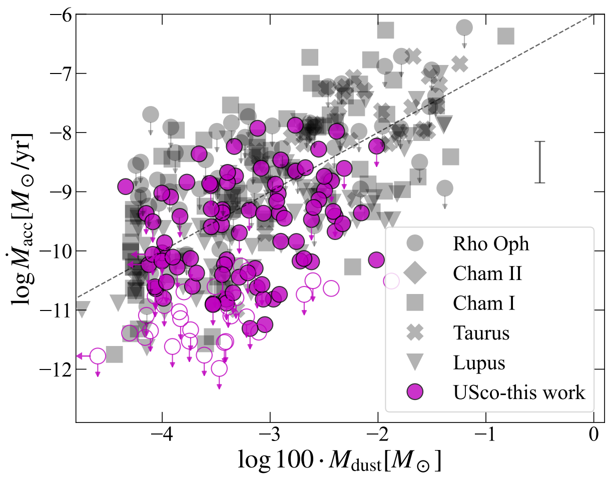

Fig. 11. $\dot{M}_{\rm acc}$ as a function of $M_{\rm disc}$ for this sample alongside values for the younger star-forming regions: ρ Ophiuchus (L1688), Chamaeleon (Cham) I and II, Lupus, and Taurus. Data are from Manara et al. (2023). The dashed grey line shows a disc lifetime ($\tau_{\rm acc} = M_{\rm disc}/\dot{M}_{\rm acc}$) of 1 Myr to guide the eye. The grey error bar represents the typical uncertainty in $\dot{M}_{\rm acc}$.

conclusions. Larger sample sizes with high-resolution ALMA data are required to better understand the effects of these objects in the $\dot{M}_{\rm acc}$–$M_{\rm disc}$ relation.

5.4. Comparison of USco with other regions

Comparison of the best fit-power laws shown in Sect. 4 with those reported for other star-forming regions suggests that USco is similar to its younger counterparts. The dependence of $L_{\rm acc}$ on $L_\star$ shows the strongest correlation in our sample, with $\rho = 0.5 \pm 0.1$ and $\beta = 2.1 \pm 0.4$. This dependence is similar to that reported for Lupus by Alcalá et al. (2017), who also report a lack of strong accretors at low stellar luminosities ($L_{\rm acc} \leq 0.1\,L_\star$). The correlation between mass accretion rate and stellar mass in our sample is also similar to those measured in Lupus, ρ Ophiuchus (L1688), and Chameleon I (β = 1.6, 1.8, and 2.3 Testi et al. 2022). However, the lower α value of -9.1 ± 0.3 in our sample suggests that the overall mass accretion rates are statistically lower, possibly reflecting the expected age dependence. This is illustrated in Fig. 10, where the values of this sample are plotted alongside those reported for the other regions by Manara et al. (2023).

Some similarities extend to the $\dot{M}_{\rm acc}$–$M_{\rm disc}$ relation. Figure 11 shows that the measurements are generally consistent with those of the other regions and show no obvious separation with age. However, the strongest accretors in our sample have lower $\dot{M}_{\rm acc}$ values than those in other regions. The range of measured disc masses is also smaller in USco, with a cut-off at $\sim 10^{-2}\,M_\odot$. Figure 12 illustrates the similarity between the best-fit slopes in Lupus, Chameleon I and our USco sample; all of which have $\beta \sim 1.0$. However, although the correlation coefficient remains similar in the two younger regions ($\rho \sim 0.7$), it is significantly weaker in USco ($\rho \sim 0.4$), indicating a significant shift in the strength of the correlation.

Although the best-fit $\dot{M}_{\rm acc}$ on $M_\star$ and $M_{\rm disc}$ relations in USco are not indifferent to those found in the younger star-forming regions, the large spread in the data suggests a different story. A consistent feature of the results is the large dispersions in the measured properties of USco. Figures 4 and 5 show, for example, that in a given $M_\star$ or $M_{\rm disc}$ bin, $\dot{M}_{\rm acc}$ varies by more than four orders of magnitude. Similar large spreads are observed in the $L_{\rm acc}$–$L_\star$ and $\dot{M}_{\rm acc}$–$R_{\rm CO}$ relations. The significance of these are reflected in the poorly measured correlations, all of which have $\rho \leq 0.5$. Moreover, the $\dot{M}_{\rm acc}$ on $R_{\rm CO}$ relation is the weakest in the sample. A β value of 0.0 ± 0.8 together with $\rho = 0.0 \pm 0.1$ indicates that these two measurements are not related. Across all relations, the magnitude of the spreads in USco are at least equal to, and generally larger than, those reported for younger regions (Alcalá et al. 2014, 2017; Testi et al. 2022), whereas the correlations are weaker (Fig. 12). Together with the larger dispersion (σ), this indicates that we are witnessing the disappearance of the relations in USco, particularly between $\dot{M}_{\rm acc}$ and $M_{\rm disc}$. The lack of a clear dependence of $\dot{M}_{\rm acc}$ on $M_{\rm disc}$ or $R_{\rm CO}$ suggests that the amount of material in the disc has no relevance to the amount of ongoing accretion implying a true disconnect between the inner and outer discs at the USco stage.

5.5. Implications for disc evolution

The accretion and disc properties in USco are believed to be an important factor in disentangling which mechanisms govern the evolution of protoplanetary discs. Although an in-depth analysis of the implications for evolutionary models is beyond the scope of this paper, we discuss briefly discuss our results in this context.

A key feature of the results in USco is the large spread of accretion rates and the weak correlations between accretion and the stellar or disc properties. This result, particularly when shown to be larger than that observed in the younger star-forming regions, contrasts with the expectations of viscous evolution theories. Under this prescription, the spread in the relations is expected to diminish over time, with values converging onto their theoretical isochrones (Lodato et al. 2017; Somigliana et al. 2024). This also predicts a changing slope in the power laws with the age of the region, which is not what we observe when we compare our sample with the younger regions. It further suggests that viscous theory alone cannot explain what we see in USco (e.g. Anania et al. 2025).

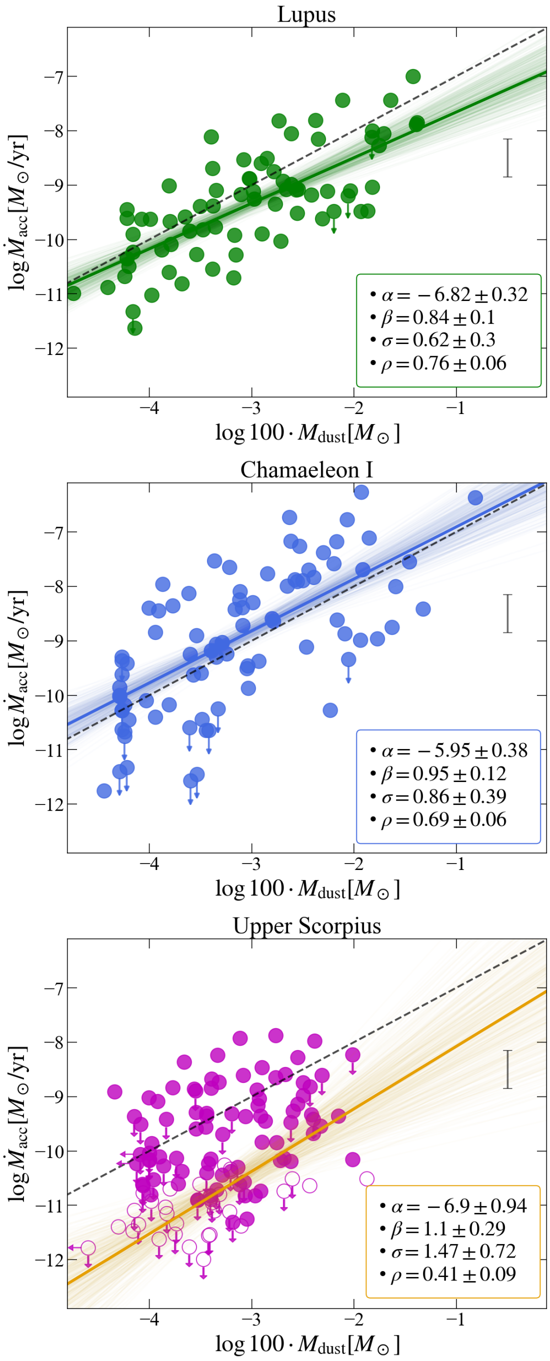

Fig. 12. $\dot{M}_{\rm acc}$ as a function of $M_{\rm disc}$ for the Lupus, Chamaeleon I and USco star-forming regions. Values for Lupus and Chamaeleon I are taken from Manara et al. (2023) while the USco sample is presented in this work. In all panels the relations are fitted using the *linmix* python package (Kelly 2007). The fit parameters for each region are shown in the text boxes of each subplot. The dashed black line represents the ratio $\tau_{\rm acc}$ = 1.0 Myr. The grey error bar represents the typical uncertainty in $\dot{M}_{\rm acc}$.

Alternatively, wind-driven models reproduce the large spreads observed in USco more successfully. Following the initial tests by Mulders et al. (2017) to reproduce the observations in Lupus, Tabone et al. (2022) showed that MHD wind-driven models reproduce the observed $\dot{M}_{\rm acc}$–$M_{\rm disc}$ spread in Lupus. This was later also tested in USco, but the agreement was dependent on the initial conditions. Tabone et al. (2025) find that reproducing the trends observed in the AGE-PRO survey requires initially compact discs with medium mass-loss rates and short accretion timescales. In contrast to viscous models, Somigliana et al. (2024) show that the slopes of the power-law relations remain the same, but that the shapes change in the wind-driven scenario. These models also reveal a larger spread in the disc lifetimes at later stages. Although neither approach reproduces the general properties of all the observed star-forming regions, the wind-driven model provides a better match to the M20 results and is more consistent with our observations. Furthermore, although wind-driven models can somewhat reproduce the lack of a correlation in the relations, they currently do not explain how one can diminish over time.

Additional processes, such as external photoevaporation (Rosotti et al. 2017), must also be considered to better account for the measured properties in the region. The moderate levels of far-ultraviolet (FUV) flux experienced by USco discs (approximately 2–12 G_0; Anania et al. 2025) have been proposed to explain the smaller average gas disc radii (Zagaria et al., in prep.). Hybrid models that include the effects of photoevaporation reproduce the disc gas sizes and disc fractions in USco more successfully. However, they still struggle to simultaneously predict accretion rates and disc masses. The evolution of dust properties is another important factor, as suggested by M20. The results from the AGE-PRO large programme show that gas and dust properties evolve differently, and that dust mass is not an ideal tracer of disc mass, particularly at older ages. Incorporating dust evolution into the viscous models of Sellek et al. (2020) improved agreement with the observed spreads in mass accretion rate and disc dust mass in USco and Lupus. Nevertheless, the current models fail to explain the full range of properties measured in USco, particularly the large spreads that we report here. Further work is required to include photoevaporation and dust evolution in evolutionary models.

Overall, the results for USco challenge the predictions of both viscous and wind-driven evolutionary scenarios. In particular, the large spreads observed in the region, characterised by its older age, is a standout feature that requires further modelling efforts to understand. In addition, a more complete sample of the gas properties of USco discs is needed to unravel the different evolutionary scenarios.

6. Summary and conclusions

In this work we present the results of a spectroscopic survey measuring the stellar and accretion properties for 127 disc-bearing stars in the USco star-forming region. By analysing their X-Shooter spectra with the multicomponent fitting code FRAPPE (Claes et al. 2024), we derive the stellar properties together with their accretion luminosity and mass accretion rates from the UV continuum excess emission. By combining these measurements with ALMA flux densities and CO disc radii (Carpenter et al. 2025; Zagaria et al., in prep.), we present the first large catalogue of USco stellar, accretion, and disc properties. We performed a statistical analysis of several key relations between these properties and fitted them with power laws, placing the results in the context of those from younger star-forming regions. We summarise the main findings of our work below:

– We applied a novel approach to determine upper limits on the accretion luminosities based on the S/N of the Balmer continua in the X-Shooter spectra. By calculating $+1\sigma$ upper limit value on $L_{\rm acc}$ we systematically distinguish between definite accretors and those with upper-limit measurements.
– Approximately 50% of the objects have a clearly measured accretion luminosity from the UV excess emission (definite

accretors). For the remaining 50% we can only determine an upper limit on L_{acc} (upper-limit accretors). This is due to the excess being intrinsically very low, non-existent, or because the S/N of the observations is poor. For a number of objects, the measured excess is below the value expected from chromospheric emission for stars of the same spectral type. These upper-limit accretors are distributed across the full range of $M_\star$, $L_\star$, and M_{disc} values.
- We analysed the relations between accretion and stellar properties. A key result is the large spread (approximately four orders of magnitude in L_{acc}), with a number of strong accretors ($L_{acc} \geq 0.1 \cdot L_\star$) along with low upper-limit accretors. Power-law fits yield low values of the correlation coefficient ($\rho \sim 0.4$–0.5) in the L_{acc}–$L_\star$ and $\dot{M}_{acc}$–$M_\star$ relations. In addition, analysis of the dependence of accretion on disc properties (dust mass and gaseous disc radii) shows that these correlations are even weaker.
- The relations between accretion and stellar properties are, in general, consistent with those of other star-forming regions (e.g. Lupus, ρ Ophiuchus, and Chamaeleon I). However, the spreads observed in USco are significantly larger than in its younger counterparts, especially when the disc properties are included. Together with the absence of a correlation between $\dot{M}_{acc}$ and disc dust mass or radius, this suggests a fading of the relations with age and that the inner and outer disc become increasingly decoupled by the age of USco (~5–10 Myr).
- These results could not be explained by membership of the objects to the various USco subgroups (Ratzenböck et al. 2023b). Similarly, the presence of (known) transition discs and binary systems was found to not affect the results.

The wealth of information contained in the X-Shooter spectra of this sample will provide more information on the properties of the USco region. Ongoing work (Empey et al., in preparation) will characterise the permitted and forbidden emission lines to further shed light on the accretion properties, chromospheric contamination, and the strength and origin of disc winds. Future work should focus on characterising the gas properties of disc-bearing stars in USco to further build upon the current understanding of the region and its role in the overall evolutionary pathway. Complementing this with additional modelling of dust evolution and photoevaporation alongside evolutionary models, would also be highly beneficial.

Data availability

Tables D.1 and E.1 are available at the CDS via `https://cdsarc.cds.unistra.fr/viz-bin/cat/J/A+A/712/A222`

Acknowledgements. We thank the anonymous referee for their careful consideration and comments that helped improve the clarity of our work. A.E. acknowledges funding from Taighde Éireann – Research Ireland under Grant number GOIPG/2023/4396 and the UCD Physics Scholarship in Research and Teaching (SIRAT). A.E. acknowledges support from the ESO Early-Career Scientific Visitor Programme when part of this work was carried out. CFM and KM are funded by the European Union (ERC, WANDA, 101039452). Views and opinions expressed are however those of the author(s) only and do not necessarily reflect those of the European Union or the European Research Council Executive Agency. Neither the European Union nor the granting authority can be held responsible for them. NOIRLab IRAF is distributed by the Community Science and Data Center at NSF NOIRLab, which is managed by the Association of Universities for Research in Astronomy (AURA) under a cooperative agreement with the U.S. National Science Foundation. GL acknowledges support from PRIN-MUR 20228JPA3A, from the European Union Next Generation EU, CUP:G53D23000870006. JMA and BN acknowledge financial support from Large Grant INAF-2024 "Spectral Key features of Young stellar objects: Wind-Accretion LinKs Explored in the infraRed (SKYWALKER).

References

Akeson, R. L., Jensen, E. L. N., Carpenter, J., et al. 2019, ApJ, 872, 158
Alcalá, J. M., Natta, A., Manara, C. F., et al. 2014, A&A, 561, A2
Alcalá, J. M., Manara, C. F., Natta, A., et al. 2017, A&A, 600, A20
Alexander, R., Pascucci, I., Andrews, S., Armitage, P., & Cieza, L. 2014, in Protostars and Planets VI, eds. H. Beuther, R. S. Klessen, C. P. Dullemond, & T. Henning, 475
Almendros-Abad, V., Manara, C. F., Testi, L., et al. 2024, A&A, 685, A118
Anania, R., Rosotti, G. P., Gárate, M., et al. 2025, ApJ, 989, 8
Anderson, K. R., Adams, F. C., & Calvet, N. 2013, ApJ, 774, 9
Andrews, S. M., Rosenfeld, K. A., Kraus, A. L., & Wilner, D. J. 2013, ApJ, 771, 129
Ansdell, M., Williams, J. P., van der Marel, N., et al. 2016, ApJ, 828, 46
Ansdell, M., Williams, J. P., Manara, C. F., et al. 2017, AJ, 153, 240
Ansdell, M., Williams, J. P., Trapman, L., et al. 2018, ApJ, 859, 21
Bai, X.-N. 2016, ApJ, 821, 80
Bai, X.-N., & Stone, J. M. 2013, ApJ, 769, 76
Bailer-Jones, C. A. L., Rybizki, J., Fouesneau, M., Demleitner, M., & Andrae, R. 2021, AJ, 161, 147
Baraffe, I., Homeier, D., Allard, F., & Chabrier, G. 2015, A&A, 577, A42
Barenfeld, S. A., Carpenter, J. M., Ricci, L., & Isella, A. 2016, ApJ, 827, 142
Barenfeld, S. A., Carpenter, J. M., Sargent, A. I., et al. 2019, ApJ, 878, 45
Betti, S. K., Follette, K. B., Ward-Duong, K., et al. 2023, AJ, 166, 262
Blandford, R. D., & Payne, D. G. 1982, MNRAS, 199, 883
Cardelli, J. A., Clayton, G. C., & Mathis, J. S. 1989, ApJ, 345, 245
Carpenter, J. M., Ricci, L., & Isella, A. 2014, ApJ, 787, 42
Carpenter, J. M., Esplin, T. L., Luhman, K. L., Mamajek, E. E., & Andrews, S. M. 2025, ApJ, 978, 117
Cazzoletti, P., Manara, C. F., Baobab Liu, H., et al. 2019, A&A, 626, A11
Cieza, L. A., Ruíz-Rodríguez, D., Hales, A., et al. 2019, MNRAS, 482, 698
Claes, R. A. B., Campbell-White, J., Manara, C. F., et al. 2024, A&A, 690, A122
Clarke, C. J. 2007, MNRAS, 376, 1350
Clarke, C. J., & Pringle, J. E. 1993, MNRAS, 261, 190
Cody, A. M., & Hillenbrand, L. A. 2018, AJ, 156, 71
Cox, E. G., Harris, R. J., Looney, L. W., et al. 2017, ApJ, 851, 83
Cuello, N., Ménard, F., & Price, D. J. 2023, Eur. Phys. J. Plus, 138, 11
Delfini, L., Vioque, M., Ribas, Á., & Hodgkin, S. 2025, A&A, 699, A145
Drążkowska, J., Bitsch, B., Lambrechts, M., et al. 2023, ASP Conf. Ser., 534, 717
Empey, A., Garcia Lopez, R., Natta, A., et al. 2025, A&A, 704, A10
Espaillat, C., Muzerolle, J., Najita, J., et al. 2014, in Protostars and Planets VI, eds. H. Beuther, R. S. Klessen, C. P. Dullemond, & T. Henning, 497
Facchini, S., Clarke, C. J., & Bisbas, T. G. 2016, MNRAS, 457, 3593
Fang, M., & Herczeg, G. J. 2025, ApJ, 994, 248
Fang, M., Pascucci, I., Edwards, S., et al. 2023, ApJ, 945, 112
Fedele, D., van den Ancker, M. E., Henning, T., Jayawardhana, R., & Oliveira, J. M. 2010, A&A, 510, A72
Fitzpatrick, M., Placco, V., Bolton, A., et al. 2025, ASP Conf. Ser., 541, 461
Franchini, M., Morossi, C., & Malagnini, M. L. 1998, ApJ, 508, 370
Freudling, W., Romaniello, M., Bramich, D. M., et al. 2013, A&A, 559, A96
Gaia Collaboration (Prusti, T., et al.) 2016, A&A, 595, A1
Gaia Collaboration (Vallenari, A., et al.) 2023, A&A, 674, A1
Gullbring, E., Hartmann, L., Briceño, C., & Calvet, N. 1998, ApJ, 492, 323
Gupta, A., Miotello, A., Manara, C. F., et al. 2023, A&A, 670, L8
Hart, K., Shappee, B., Hey, D., et al. 2023, arXiv e-prints [arXiv:2304.03791]
Hartmann, L., Herczeg, G., & Calvet, N. 2016, ARA&A, 54, 135
Hendler, N., Pascucci, I., Pinilla, P., et al. 2020, ApJ, 895, 126
Herczeg, G. J., & Hillenbrand, L. A. 2014, ApJ, 786, 97
Houdebine, E. R., Mathioudakis, M., Doyle, J. G., & Foing, B. H. 1996, A&A, 305, 209
Ingleby, L., Calvet, N., Bergin, E., et al. 2011, ApJ, 743, 105
Ingleby, L., Calvet, N., Hernández, J., et al. 2014, ApJ, 790, 47
Kausch, W., Noll, S., Smette, A., et al. 2015, A&A, 576, A78
Kelly, B. C. 2007, ApJ, 665, 1489
Lesur, G. 2021, J. Plasma Phys., 87, 205870101
Lodato, G., Scardoni, C. E., Manara, C. F., & Testi, L. 2017, MNRAS, 472, 4700
Long, F., Herczeg, G. J., Harsono, D., et al. 2019, ApJ, 882, 49
Luhman, K. L. 2020, AJ, 160, 186
Luhman, K. L., & Mamajek, E. E. 2012, ApJ, 758, 31
Lynden-Bell, D., & Pringle, J. E. 1974, MNRAS, 168, 603
Manara, C. F. 2014, Ph.D. Thesis, Ludwig-Maximilians University of Munich, Germany
Manara, C. F., Beccari, G., Da Rio, N., et al. 2013a, A&A, 558, A114

Manara, C. F., Testi, L., Rigliaco, E., et al. 2013b, A&A, 551, A107
Manara, C. F., Testi, L., Natta, A., et al. 2014, A&A, 568, A18
Manara, C. F., Fedele, D., Herczeg, G. J., & Teixeira, P. S. 2016a, A&A, 585, A136
Manara, C. F., Rosotti, G., Testi, L., et al. 2016b, A&A, 591, L3
Manara, C. F., Testi, L., Herczeg, G. J., et al. 2017, A&A, 604, A127
Manara, C. F., Mordasini, C., Testi, L., et al. 2019, A&A, 631, L2
Manara, C. F., Natta, A., Rosotti, G. P., et al. 2020, A&A, 639, A58
Manara, C. F., Frasca, A., Venuti, L., et al. 2021, A&A, 650, A196
Manara, C. F., Ansdell, M., Rosotti, G. P., et al. 2023, ASP Conf. Ser., 534, 539
Maucó, K., Manara, C. F., Ansdell, M., et al. 2023, A&A, 679, A82
Miotello, A., Kamp, I., Birnstiel, T., Cleeves, L. C., & Kataoka, A. 2023, ASP Conf. Ser., 534, 501
Modigliani, A., Goldoni, P., Royer, F., et al. 2010, SPIE Conf. Ser., 7737, 773728
Morbidelli, A., & Raymond, S. N. 2016, J. Geophys. Res.: Planets, 121, 1962
Mulders, G. D., Pascucci, I., Manara, C. F., et al. 2017, ApJ, 847, 31
Najita, J. R., Strom, S. E., & Muzerolle, J. 2007, MNRAS, 378, 369
Najita, J. R., Andrews, S. M., & Muzerolle, J. 2015, MNRAS, 450, 3559
Pascucci, I., Testi, L., Herczeg, G. J., et al. 2016, ApJ, 831, 125
Pascucci, I., Cabrit, S., Edwards, S., et al. 2023, ASP Conf. Ser., 534, 567
Pascucci, I., Beck, T. L., Cabrit, S., et al. 2025, Nat. Astron., 9, 81
Pfalzner, S., Vogel, P., Scharwächter, J., & Olczak, C. 2005, A&A, 437, 967
Pinilla, P., Sierra, A., Kurtovic, N. T., et al. 2025, MNRAS, 543, 2723
Preibisch, T., Brown, A. G. A., Bridges, T., Guenther, E., & Zinnecker, H. 2002, AJ, 124, 404
Ratzenböck, S., Großschedl, J. E., Alves, J., et al. 2023a, A&A, 678, A71
Ratzenböck, S., Großschedl, J. E., Möller, T., et al. 2023b, A&A, 677, A59
Rigliaco, E., Natta, A., Testi, L., et al. 2012, A&A, 548, A56
Rizzuto, A. C., Ireland, M. J., & Kraus, A. L. 2015, MNRAS, 448, 2737
Rogers, C., de Marchi, G., & Brandl, B. 2025, A&A, 698, A172
Rosotti, G. P., Clarke, C. J., Manara, C. F., & Facchini, S. 2017, MNRAS, 468, 1631
Sanchis, E., Testi, L., Natta, A., et al. 2020, A&A, 633, A114
Sellek, A. D., Booth, R. A., & Clarke, C. J. 2020, MNRAS, 498, 2845
Shappee, B. J., Prieto, J. L., Grupe, D., et al. 2014, ApJ, 788, 48
Siess, L., Dufour, E., & Forestini, M. 2000, A&A, 358, 593
Smette, A., Sana, H., Noll, S., et al. 2015, A&A, 576, A77
Somigliana, A., Testi, L., Rosotti, G., et al. 2024, A&A, 689, A285
Stelzer, B., Frasca, A., Alcalá, J. M., et al. 2013, A&A, 558, A141
Tabone, B., Rosotti, G. P., Lodato, G., et al. 2022, MNRAS, 512, L74
Tabone, B., Rosotti, G. P., Trapman, L., et al. 2025, ApJ, 989, 7
Testi, L., Natta, A., Manara, C. F., et al. 2022, A&A, 663, A98
Tody, D. 1986, SPIE Conf. Ser., 627, 733
Tody, D. 1993, ASP Conf. Ser., 52, 173
Towner, A. P. M., Eisner, J. A., Sheehan, P. D., Hillenbrand, L. A., & Wu, Y.-L. 2026, ApJ, 999, 145
van der Marel, N. 2023, Eur. Phys. J. Plus, 138, 225
Vernet, J., Dekker, H., D'Odorico, S., et al. 2011, A&A, 536, A105
Vioque, M., Kurtovic, N. T., Trapman, L., et al. 2025, ApJ, 989, 9
Vorobyov, E. I., & Basu, S. 2009, ApJ, 703, 922
Winter, A. J., & Haworth, T. J. 2022, Eur. Phys. J. Plus, 137, 1132
Winter, A. J., Benisty, M., Manara, C. F., & Gupta, A. 2024, A&A, 691, A169
Xie, C., Pascucci, I., Long, F., et al. 2026, AJ, accepted [arXiv:2606.27477]
Zagaria, F., Clarke, C. J., Rosotti, G. P., & Manara, C. F. 2022, MNRAS, 512, 3538
Zagaria, F., Facchini, S., Miotello, A., et al. 2023, A&A, 672, L15
Zallio, L., Rosotti, G., Tabone, B., et al. 2024, A&A, 692, A93
Zallio, L., Rosotti, G. P., Vioque, M., et al. 2026a, A&A, 705, A49
Zallio, L., Vioque, M., Andrews, S. M., et al. 2026b, A&A, 708, L1
Zhang, K., Pérez, L. M., Pascucci, I., et al. 2025, ApJ, 989, 1

[1] University College Dublin (UCD), Belfiled, Dublin, Ireland
[2] European Southern Observatory, Karl-Schwarzschild-Strasse 2, 85748 Garching bei München, Germany
[3] School of Cosmic Physics, Dublin Institute for Advanced Studies, 31 Fitzwilliams Place, Dublin 2, Ireland
[4] Max Planck Institute for Astronomy, Königstuhl 17, 69117 Heidelberg, Germany
[5] Institue of Astronomy, University of Cambridge, Madingley Road, Cambridge CB3 OHA, UK
[6] INAF-Osservatorio Astronomico di Capodimonte, via Moiariello 16, 80131 Napoli, Italy
[7] School of Physics, Trinity College Dublin, the University of Dublin, College Green, Dublin 2, Ireland
[8] Joint ALMA Observatory, Avenida Alonso de Córdova 3107, Vitacura, Santiago, Chile
[9] Dipartimento di Fisica, Università degli Studi di Milano, Via Celoria 16, 20133 Milano, Italy
[10] INAF-Osservatorio Astrofisico di Arcetri, Largo E. Fermi 5, I-50125 Firenze, Italy
[11] Universidad Nacional Autónoma de México, Instituto de Astronomía, AP 106, Ensenada 22800, BC, México
[12] INAF – Osservatorio Astronomico di Roma, Via di Frascati, 33, 00078 Monte Porzio Catone, Italy
[13] Lunar and Planetary Laboratory, the University of Arizona, Tucson, AZ 85721, USA
[14] SUPA, School of Physics & Astronomy, University of St Andrews, North Haugh, St Andrews KY16 9SS, UK
[15] Alma Mater Studiorum – Università di Bologna, Dipartimento di Fisica e Astronomia "Augusto Righi", Via Gobetti 93/2, I-40129 Bologna, Italy
[16] Department of Physics, Maynooth University, Maynooth, Co. Kildare, Ireland

Appendix A: Derivation of upper limits

Among the USco sample we record a significant number of very low values of accretion luminosity measured from their UV continuum excess with FRAPPE. In many cases these are on or below the sensitivity limit of what can be reliably measured from the X-Shooter spectra. To allow for an accurate statistical analysis of the region, there is a need to distinguish between definite measurements of excess due to accretion and those which are upper limits. In this study we develop a novel approach to separating such measurements based on the S/N ratio in the Balmer continua of the observed spectra, while also calculating $+1\sigma$ upper limits on the accretion luminosity. In this section we describe the procedure we follow to do this.

For each object we first correct the X-Shooter spectrum for interstellar extinction using the best fit value of A_V determined by FRAPPE, and the Cardelli extinction law (Cardelli et al. 1989) with $R_V = 3.1$. With this we compute the mean value and a 1 σ RMS for four bins in the Balmer continuum ($\lambda\lambda$ 332.5 - 337.5 nm, 337.5 - 342.5 nm, 352 - 358 nm, 359 - 362 nm). These are the same wavelength ranges used by FRAPPE in the fit to constrain the accretion excess. A relative uncertainty was then defined by taking the average ratio of the $+1\sigma$ RMS to the mean flux across all bins. The uncertainties associated with the interpolated class III template fitted by FRAPPE are negligible compared to the noise in the observed spectra, therefore they not considered in this analysis. This final value represents the uncertainty on the flux of the observed Balmer continuum, and therefore that of the excess due to accretion. This fractional excess was applied to the observed (uncorrected) Balmer continuum flux (332.5-362.0 nm) to create a $+1\sigma$ artificial spectrum. For each object the analysis with FRAPPE was reran on the artificial spectrum with a fixed input SpT and A_V (those initially derived, and reported in Table D.1). This leaves the excess due to accretion as the only free parameter in the fitter, and hence from the resulting fit we obtain a $+1\sigma$ value of the accretion luminosity. For each target we compare this with the original value of $L_{\rm acc}$. A given object was determined to be an upper-limit measurement if the relative difference between the measured accretion luminosity ($L^{\rm M}_{\rm acc}$) and the one obtained artificially ($+1\sigma$), as just described, ($L^{\rm UL}_{\rm acc}$) exceeded 20%. Mathematically this is:

$$\frac{L^{\rm UL}_{\rm acc} - L^{\rm M}_{\rm acc}}{L^{\rm M}_{\rm acc}} > 0.2. \tag{A.1}$$

The choice of 20% as a threshold was determined empirically by assessing a range of values and comparing the resulting classifications (upper-limit or definite accretion measurements) with a visual inspection of the FRAPPE fits. A value of 20% provided the best agreement, minimizing both false upper limits and misclassified definite accretors. As a secondary check, we also inspect the equivalent widths (EW) of the H_α and compare them to the classical threshold of 10 Å. Of the targets showing a clear excess, 86% (61/71) have EWs ≥10Å; nine of the remaining ten have EW < 10Å while one target doesn't have a clear emission line profile (2MASS J116101264-2104446). For upper-limit accretion measurements, just under half (45%, 22/49) have EWs ≥ 10Å, with all the others showing EWs < 10 Å. Objects which were deemed to have upper-limit measurements by the method described above, are indicated by a 'y' in the upper limit (UL) column of Tab. D.1, and an 'n' if they show a reliable continuum excess.

Under the approach described above, a measurement of $L_{\rm acc}$ has an upper-limit detection if either its spectrum has a poor S/N in the UV continuum, leading to difficulty in detecting accretion excesses or there remains no clear excess even with a good S/N. These are important factors to consider when evaluating the statistics of the sample (see Sect. 4). Following this method we find that 49/121 targets have upper limit-accretion measurements (these are indicated by a "y" in the upper limit (UL) column of Table D.1 and identified with a downward pointing arrow in any plots of $L_{\rm acc}$ or $\dot{M}_{\rm acc}$. Figure A.1 shows the X-Shooter spectrum and FRAPPE fits for two examples, one for a upper-limit measurement (J16253798-1943162) and one for a true detection (J15590484-2422469).

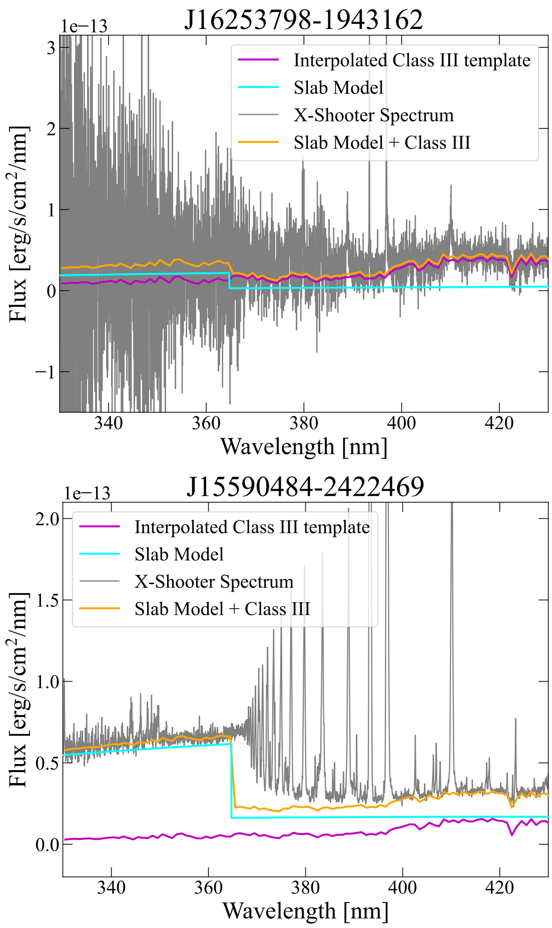

Fig. A.1. Examples of the FRAPPE fits for upper-limit and definite accretors. In both plots, the de-reddened X-Shooter spectrum is plotted in grey, the interpolated class III template in magenta, in cyan the best fit isothermal hydrogen slab model, and in orange the class III template + slab model. On the left is an object defined as an upper-limit accretor based on its low S/N in the UV. On the right is a definite accretor where the UV continuum excess is clear.

Appendix B: Stellar variability

As described in Section 2.3, the synthetic magnitudes of all the objects in the sample were compared with historical photometric measurements. Most were in good agreement; however, a subsample of seven targets showed significant differences. These differences are believed to be due to variability of the central star. All seven show g or V band variability of at least 1 magnitude in their lightcurves on the ASAS-SN Sky Patrol database (Shappee et al. 2014; Hart et al. 2023). Two objects (2MASS J16222160-2217307, 2MASS J16253849-2613540) were additionally classified as dippers and one as a stochastic variable star (2MASS J16020429-2231468) by Cody & Hillenbrand (2018).

We exclude just the latter object from the analysis due to uncertainty in its derived properties. While the comparison with photometry shows a difference of around 0.6 mag in the Gaia filters, the results from FRAPPE are also uncertain. We measure an extremely low $L_\star$ for its associated $T_{\rm eff}$, which does not fall within the available evolutionary tracks on the HR diagram (Fig. 1). Cody & Hillenbrand (2018) measured a particularly high variability amplitude (0.91 of its normalised flux). The ASAS-SN light curve showed maximum variations of 3 magnitudes in the g filter. It is possible that this object was caught during an active period while undergoing some form of unpredictable variability. Additionally, having a highly inclined disc can result in an obscured photosphere, leading to an underestimated value of its stellar luminosity (Alcalá et al. 2014). Follow-up observations would be required to verify if this is the case for this particular target. To avoid these uncertainties influencing other results, it was discounted in the analysis of the accretion and stellar properties.

Appendix C: Additional plots

For each relation considered in Section 4, as well as considering the scatter we also compute medians, 25th and 75th quantile values for bins of the independent variable. This is done while considering define accretors only and also for the whole sample (including the upper-limits accretors equally). We note that where the number of upper-limit accretors in a given bin exceeds those of the definite accretors, the true median and lower quantile are not well defined. The results of this approach are seen in Figure C.1.

In Figure C.3 the values of $L_\star$, $M_\star$, $L_{\rm acc}$, and $\dot{M}_{\rm acc}$ are compared for shared targets in this work and that of M20. Values are in general in good agreement within uncertainties. Differences in $L_{\rm acc}$, $\dot{M}_{\rm acc}$ are seen particularly in the cases of upper-limit accretors, this can be attributed to the novel approach to determining upper-limit values done in this work. A greater dispersion is also seen when comparing the stellar properties ($L_\star$, $M_\star$), particularly at the lowest masses. Such differences stem from the updates to the fitting procedure used in this work (FRAPPE) compared to the previous routine used in M20 (see Claes et al. (2024) for details). Particularly, the use of a different SpT-$T_{\rm eff}$ relation can account for the deviations in the stellar mass and luminosity between the two datasets.

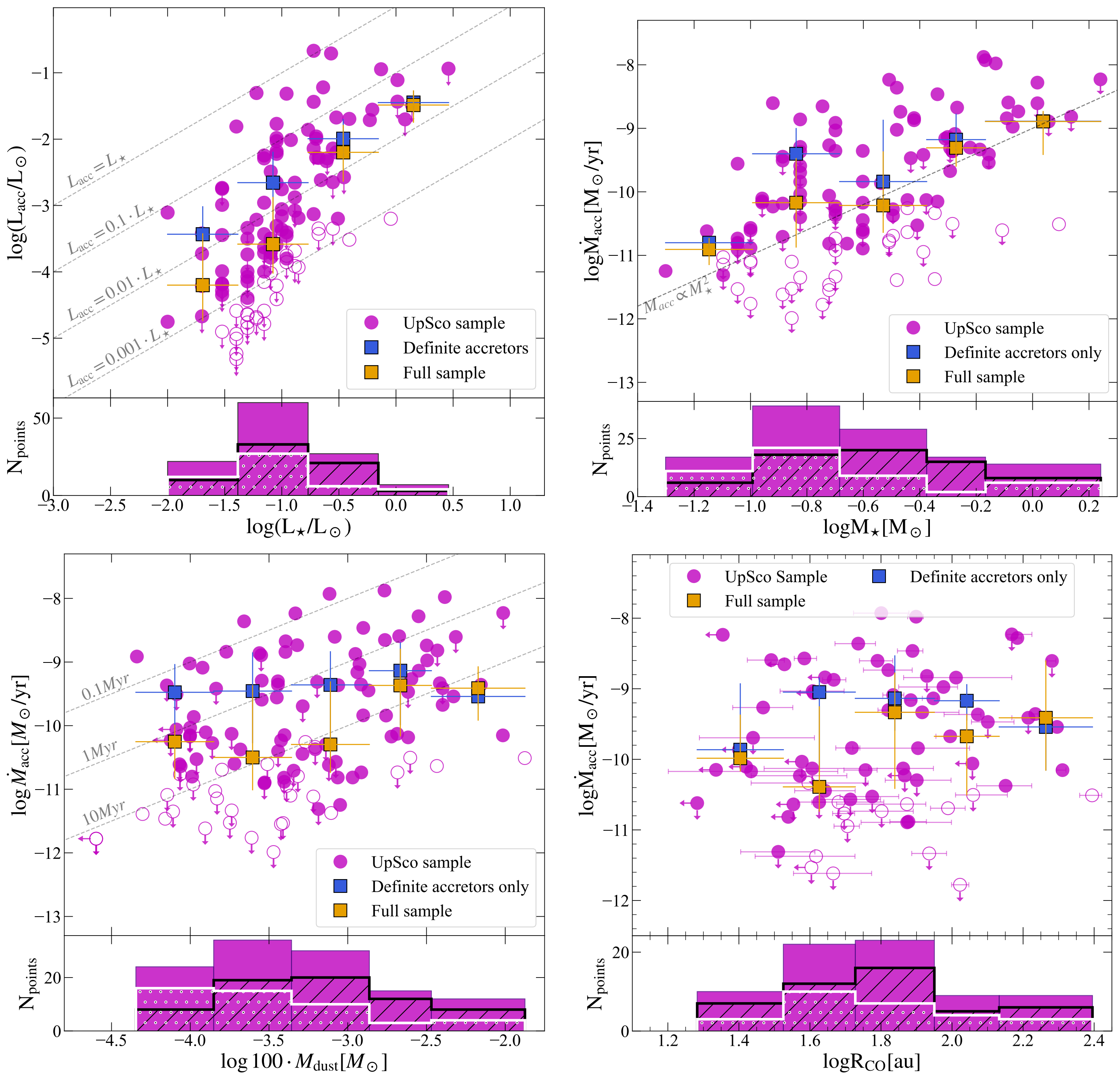

Fig. C.1. Scatter plots and histograms of stellar, disc and accretion properties for the USco sample. Squares represent the medians while vertical lines represent the limits of the 25th and 75th quantile in a given bin of $L_\star$, $M_\star$, $\dot{M}_{\rm acc}$, $M_{\rm disc}$, and $R_{\rm CO}$. Horizontal lines are indicative of the width of given bin. Blue medians and quantiles are computed for definite accretors only (solid points, no arrow), orange squares and lines are for the full sample (including upper limits, treated equally). We note for bins where the number of upper-limit accretors exceed the number of definite accretors the median and quantile values are not well defined. Bottom panel: histograms of the full sample (magenta), upper limits only (white dotted), and detections only (black striped) in each bin. . From top left: $L_{\rm acc}$ vs $L_\star$, $\dot{M}_{\rm acc}$ vs $M_\star$, $\dot{M}_{\rm acc}$ vs $M_{\rm disc}$, and $\dot{M}_{\rm acc}$ vs $R_{\rm CO}$.

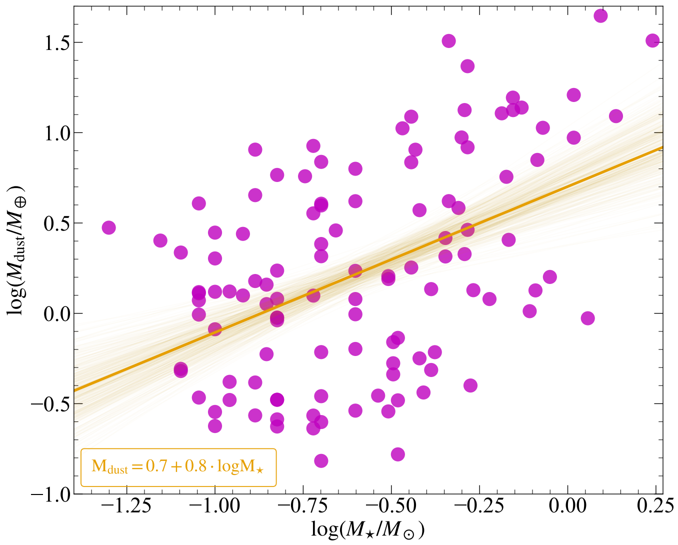

Fig. C.2. Relation of dust mass to stellar mass. The scatter plot and best fit power law follow the same convention as those in Section 4. See Table 1 for the best fit parameters determined by *linmix*.

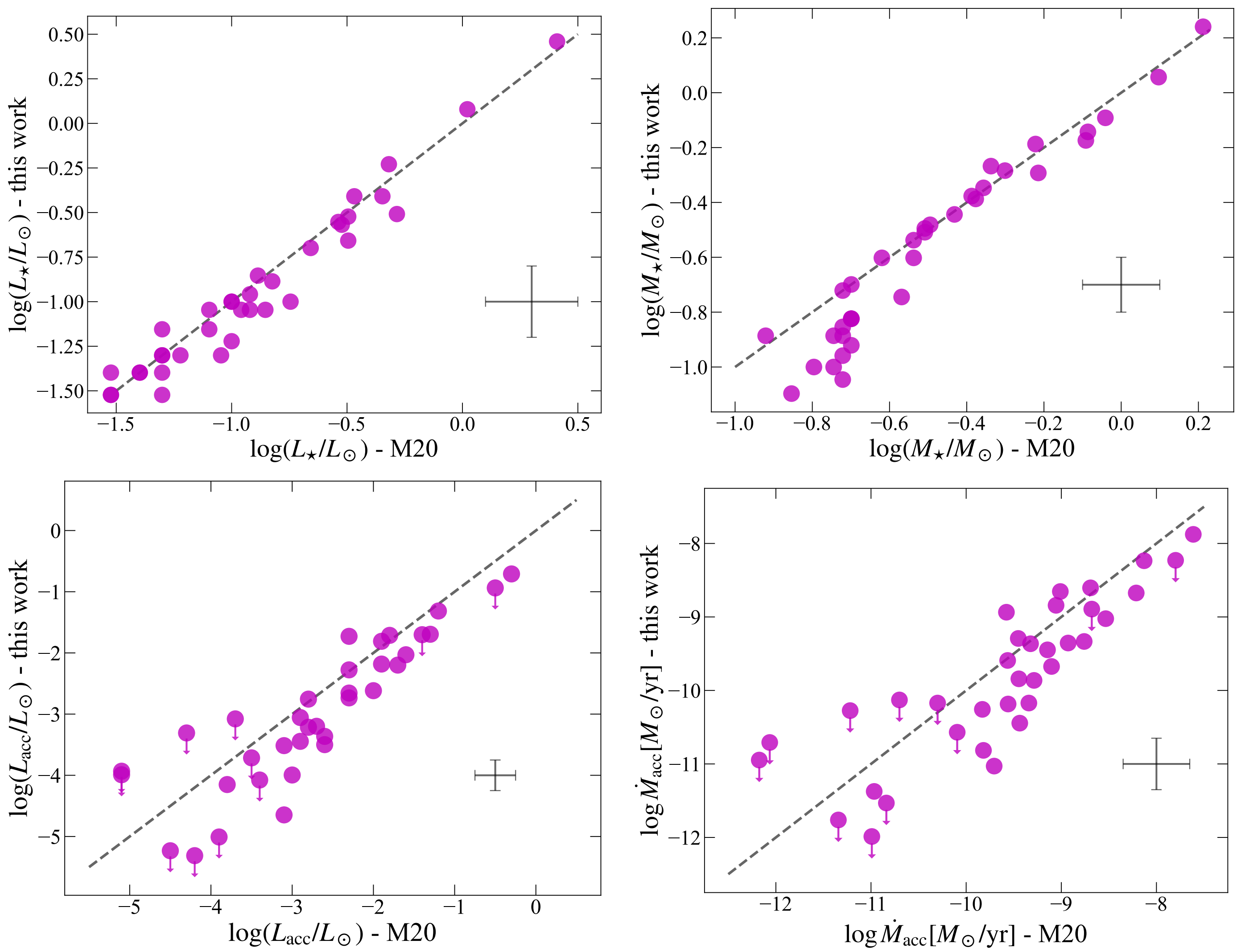

Fig. C.3. Comparison of $L_\star$, $M_\star$, $L_{\rm acc}$, and $\dot{M}_{\rm acc}$ values derived in this work and those derived in M20 for shared objects. Dashed grey lines represent a one-to-one relation. Grey error bars represent the typical uncertainties on the derived values.

Appendix D: Table of results

Table D.1. Stellar, disc and accretion properties for all objects fit with FRAPPE.

2MASS ID	SpT	Dist [pc]	T_{eff} [K]	A_V [mag]	$L_\star$ [$L_\odot$]	$M_\star$ [$M_\odot$]	Age [Myr]	logL_{acc} [$L_\odot$]	$\dot{M}_{acc}$ [$M_\odot$ yr^{-1}]	M_{dust} [$M_\odot$]	UL (y/n)	CA (y/n)
J16025431-1805300	M5.0	149.3	2980	0.7	0.05	0.10	2.13	-4.638	7.68×10^{-12}	6.04×10^{-6}	y	y
J16024152-2138245	M4.5	139.4	3085	0.4	0.03	0.13	5.40	-3.445	6.54×10^{-11}	2.42×10^{-5}	n	n
J16140792-1938292	G9.5	159.5	4947	0.9	1.38	1.37	7.98	-1.486	1.52×10^{-9}	3.71×10^{-5}	y	n
						...						
J16142029-1906481	K7.5	138.8	3960	2.5	0.19	0.74	15.36	-0.669	1.05×10^{-8}	4.13×10^{-5}	n	n

Notes. Same as above Columns 12 & 13 refer to if an object is determined to have an upper limit accretion measurement (UL) or that its $L_{acc}/L_\star$ ratio is below the expected limit for chromospheric activity (CA) (This table is available in its entirety in machine-readable form at the CDS)

Appendix E: Log of the observations

Table E.1. Night log of observations.

2MASS ID	Date of Observation [UT]	Exp. Time [Nexp x (s)]	Slit Width ["] UVB	VIS	NIR	Airmass ["]	I.Q. ["]	SNR [@ 335 nm]
J15354856-2958551_E	2018-05-19T23:39:04.373	4×300	1.0	0.4	0.4	0.42	2.22	89.8
J15354856-2958551_W	2018-05-19T23:39:04.373	4×300	1.0	0.4	0.4	0.42	2.22	57.8
J15442550-2126408	2024-07-25T00:56:53.279	4×600	1.0	0.4	0.4	0.94	1.02	166.0
		...						
J16395577-2347355	2024-05-20T09:21:49.414	4×360	1.0	0.4	0.4	1.14	1.65	69.2

(This table is available in its entirety in machine-readable form at the CDS)